JAERI-M
82-177

JAPANESE CONTRIBUTIONS TO IAEA INTOR WORKSHOP, PHASE IIA
CHAPTER X: ELECTROMAGNETICS

November 1982

Satoshi NISHIO, Koju UEDA*, Nobuharu MIKI**,
Noboru FUJISAWA, Yoshio TANABE**, Junji OHMORI**,
Mitsuharu NAGANUMA**, Yukiharu NAKAMURA
and Yoshio SAWADA**

日本原子力研究所
Japan Atomic Energy Research Institute

JAERI-Mレポートは，日本原子力研究所が不定期に公刊している研究報告書です。
入手の問合わせは，日本原子力研究所技術情報部情報資料課（〒319-11茨城県那珂郡東海村）あて，お申しこしください。なお，このほかに財団法人原子力弘済会資料センター（〒319-11 茨城県那珂郡東海村日本原子力研究所内）で複写による実費頒布をおこなっております。

JAERI-M reports are issued irregularly.
Inquiries about availability of the reports should be addressed to Information Section, Division of Technical Information, Japan Atomic Energy Research Institute, Tokai-mura, Naka-gun, Ibaraki-ken 319-11, Japan.

編集兼発行　日本原子力研究所
印　　刷　㈱高野高速印刷

JAERI-M 82-177

Japanese Contributions to IAEA INTOR Workshop, Phase II A

Chapter X : Electromagnetics

Satoshi NISHIO , Koju UEDA*, Nobuharu MIKI**,
Noboru FUJISAWA , Yoshio TANABE**, Junji OHMORI**,
Mitsuharu NAGANUMA**, Yukiharu NAKAMURA and Yoshio SAWADA**

Fusion Research and Development Center
Tokai Research Establishment, JAERI

(Received November 1, 1982)

This report corresponds to Chapter X of Japanese contribution report to IAEA INTOR workshop, Phase II A. Transitional analysis of electromagnetic phenomenon which includes joule heat depositions in supper conducting coil system, electromagnetic force acting on torus components and shell effects for stabilizing plasma positional instability, is carried out.

Keywords : INTOR, Joule Loss, Disruption, Supper Conducting Coil, Position Control, Shell Effect, Shield, Blanket, Electromagmetics

---

* On leave from Mitsubushi Electric Co.,Ltd.

** Toshiba Electric Co.,Ltd.

INTORフェーズⅡAワークショップ検討報告書
第X章：過　度　電　磁　解　析

日本原子力研究所東海研究所
核融合研究開発推進センター

西尾　敏・　上田孝寿[*]・三木信晴[**]・藤沢　登・田辺義雄[**]
大森順次[**]・長沼正光[**]・中村幸治・沢田芳夫[**]

（１９８２年１１月１日受理）

国際トカマク炉（INTOR）における過度電磁現象のうち主な関心事として，超電導コイルシステムに誘起される渦電流損失，プラズマ異常消滅時にトーラスコンポーネントに作用する電磁力およびプラズマの位置不安定さを仰えるシェル効果が挙げられる。これら現象に関する知識が炉概念の検討を進める上において，さらには詳細な設計研究を進める上において必要不可欠であることは論を待たない。

本報告書は，上記過度電磁現象を解析し今後の具体的な指針を与えるべくまとめられたものである。

＊）　外来研究員：三菱電機（株）

＊＊）　東京芝浦電気（株）

CONTENS

目　　次

Table Caption and Figure Caption

1. Introduction (Influence of electromagnetics on machine design)

In designing Tokamak reactor, the transitional analysis of electromagnetic phenomenon is commonly considered to be one of the most important studies. The induced eddy currents exert mechanical loading to the structures by the interaction with magnetic fields and the loading must be considered in the structural strength analysis. The shell effect by induced eddy currents on the torus structures play an important part in stabilizing the positional instability of a elongated plasma column. And the Joule heat depositions by the eddy currents are not negligible in the structures of the supperconducting magnet system.

Section 2. describes the effects of plasma disruption. These are the electromagnetic force acting on the torus components (first wall, pump limiter plate, blanket structure, shield structure, vacuum vessel and bellows), the induced currents and voltages in PF coils and the Joule heat generation (not only in the case of plasma disruption but also in the case of normal operation) in the coil conductors and the cryostat.

Section 3. and 4. describe the plasma positional control including the passive shell effects and the active feedback control. The plasma positional control for only vertical displacement was investigated because of the vertically elongated plasma which is intrinsically unstable in vertical direction. Various kinds of shell structures were investigated in consideration of the engineering feasibility and high tritium breeding ratio. And as is well recognized from the experimental results, the positional control with a required accuracy is indispensable in order to avoid the strong plasma-wall interaction which leads to impurity source. The feedback control was studied in consideration of the eddy currents induced in the main torus structures such as passive shell structure,

blanket box and shield structure.

Section 6. describes the methodology for analyzing the transient electromagnetic phenomena. The appropriate modeling techniques are described for each phenomenon respectively.

2. Plasma Disruption Effect

The time-varying fields caused by the plasma disruption or the PF coil operation generate the eddy currents in the first wall, the blanket, the radiation shield, the magnet cryostat and the TF coils. The interaction of eddy currents with the magnetic field leads to additional forces whose effect upon the structure may well be considerable. Also, eddy currents in structures lead to energy dissipation in these structures, which is particularly important for structures at cryogenic temperatures and thus must be accounted for in calculating the thermal load on the cryogenic system.

The plasma current disruption is assumed to occur linearly from $I_p = 6.4$ MA to zero during 20 ms. The following effects were considered:

(a) Heat generation:

Eddy currents induced in the metallic parts of the SC coils (supporting structure, frames, superconductor) lead to thermal energy dissipation in them, which threatens the thermal margin and introduces an additional source of heat to the cryogenic system.

The assessments were conducted not only for plasma disruption but also for normal operation.

(b) Force and torque:

Considerable eddy currents are induced and, because of their interaction with the magnetic field, large forces act upon the structures. However, from our examinations, it was concluded that the electromagnetic loads on the torus sectors is to an acceptable level during plasma disruption.

(c) Induced voltage:

Voltages are induced in the PF coils which lead to abrupt changes in PF coil current. From our examinations, the voltages induced in the PF coils is to an acceptable level during plasma disruption.

2.1 Heating of coils

The main effect of eddy currents upon the magnetic systems is the generation of thermal energy in the superconductor, supporting frames of coils, containers for liquid helium and the structure of the superconducting TF coil, i.e. in all the structures cooled down to a temperature of 4.2 K.

Thermal loads in the superconducting winding (SCW) result from eddy currents flowing during the whole cycle of magnetic field change. During plasma start-up or disruption, this results in adiabatic heating of the SCW. The value of the thermal loads determines the required temperature margin of the superconductor.

Heat generated in the load-bearing frames and support structure may be intercepted by cooling channels in the walls of the helium vessel. Therefore, thermal loads in the frames and the support structure lead to no adiabatic heating of the superconducting winding; they only affect helium consumption in the cooling channels and the required power of the cryogenic system.

Three cases are considered in our study:

a. Case 1: ◦ Reduced size of TF coils
   ◦ Pump limiter operation with small ring coil (Max. radius of ring coil = 11 m)

b. Case 2: ◦ Reduced size of TF coils
   ◦ Pump limiter operation with large ring coil (Max. radius of ring coil = 13 m)

c. Case 4A: ◦ Reduced size of TF coils

◦ Divertor operation with small ring coil

2.1.1 AC losses in TF coils during normal operation

The AC loss is caused by the changing poloidal field mainly at the superconductor, the helium vessel and the coil support in the TF coils.

(1) AC loss in the superconductors

In the superconductor the AC losses are composed of the hysteresis loss, the eddy current loss and the coupling loss, as listed in Table X-2-1. The coupling loss is the largest for the adopted conductor configuration such as the large matrix area. The CuNi fins are inserted in the matrix to cut the coupling current. The time averaged loss can be calculated from Table X-2-1, as follows,

P_{av} = 15.4 kW for case 1

P_{av} = 14.5 kW for case 2

P_{av} = 42.8 kW for case 4A

The averaged loss for case 4A is large, since the magnetomotive forces of No.23 and No.24 PF coils are large compared with other cases.

(2) AC loss in TF coil helium vessels

Since the helium vessel is required to withstand against the electromagnetic force, the material should be thick stainless steel. The changing poloidal field generates the eddy current loss in the ve-sel. The models for the estimation of the loss are shown in Fig.X-2-1. The time averaged loss is

P_{av} = 14.4 kW for case 1

P_{av} = 14.1 kW for case 2

P_{av} = 35.8 kW for case 4A

The loss for case 4A is large because the magnetoforce of No.23 and No.24 PF coil are large compared with other two cases.

(3) AC loss in TF coil supports

The TF coil support is placed between TF coils to with-stand the electromagnetic out-of-plane forces, and the contact face with the TF coil is covered with insulator to cut the one-turn loop. The eddy current induced by the changing poloidal field generates the loss. The model for the loss calculation is shown in Fig.X-2-1. The time averaged losses are,

P_{av} = 26.2 kW for case 1

P_{av} = 20.0 kW for case 2

P_{av} = 70.5 kW for case 4A

The loss in the supports is dominant compared with other AC losses, since the high field is applied to the support region. Therefore, it is needed that the more insulators should be inserted into the support to reduce the loss.

(4) Total AC loss in TF coils

The averaged AC losses are summerized in Table X-2-2 for each case. The loss in the coil supports is the largest, and should be reduced by putting the insulators into the supports. The loss for case 4A is about three times larger than that for the other two cases. This stems from that the magnetomotive forces of No.23 and No.24 PF coil are large compared with the other cases.

2.1.2 AC loss in TF coil due to plasma disruption

The rapidly changing magnetic field caused by the plasma disruption will generate the loss on the superconductor, the helium vessel and the coil support. First of all, the loss will be roughly overestimated with

ignoring the shielding effect by the vacuum chamber and blanket.
The losses in liquid helium vessel, the coil support and the superconductot are averaged over the duration time and summed up to about 140 kW, which can be reduced considering the shielding effect. AC loss distribution along the superconductor is shown in Fig.X-2-2.

2.1.3 AC loss is PF coils during normal operation

The PF coil is the source of changing field which holds the plasma in equilibrium, and is subject to the AC loss due to the changing field. The loss occurs in the superconductors, the coil supports and the helium leak shield if used, for PF coils. The loss can be estimated for above components, as follows.

(1) AC loss of PF coil superconductor

The superconductor has been intensively developed to reduce the AC loss. Therefore, the conductors are stranded several times and consist of mixed matrices. The superconductor AC loss is conveniently divided into three contributions, i.e. the hysteresis loss, the eddy current loss and the coupling loss. The formulae are listed in Table X-2-3. The losses for each coil are summed up taking account of the field patterns from each coil, and then, they are averaged over the duration.

P_{av} = 1.3 kW for case 1

P_{av} = 1.4 kW for case 2

P_{av} = 2.0 kW for case 4A

The coupling loss between bundles is the most modinant for the adopted conductor configuration.

(2) AC loss of PF coil supports

It is required for PF coil supports that the Ac loss should be reduced as small as possible and the supports should endure the electromagnetic forces. First of all, the supports should not electrically close to make a circle around the torus axis, otherwise the loss is vast.

The AC loss can be estimated from the following equation.

$$P = \frac{t_w}{12\rho} \int \dot{B}^2 d\ell \quad (W)$$

where, ρ is the resistivity of the support material, and the other nomenclatures are shown in Fig.X-2-3. The thickness 50 mm needed from the stress analysis, and the magnetic field corresponding to the PF coil current waveforms are inserted into the above equation. The losses of each coil are summed up and them, they are averaged over the duration.

P_{av} = 2.5 kW for case 1

P_{av} = 2.6 kW for case 2

P_{av} = 10.4 kW for case 4A

(3) AC loss in PF coil helium leak shields

The helium leak shield may be needed at the present time, since the helium leakage from the vessel is inevitable as long as the large FRP's are adopted to the vessels. It can consist of metal such as stainless steel to be sealed tightly, and therefore it is expected that the AC loss might be vast due to one turn loop, even though the thickness is as this as possible. The SS thickness of 0.5 mm is assumed in the following analysis.

The dominant loss may be the induced current loss due to the linkage flux, and obtained as follows,

$$P = \frac{\dot{\phi}^2}{R} \quad (W)$$

where, $\dot{\phi}$ is the linkage flux in the shield, R the resistance. The losses for each leak shield are summed up taking account of the field patterns, and they are averaged over the duration.

P_{av} = 20.3 kW for case 1

P_{av} = 28.9 kW for case 2

P_{av} = 43.0 kW for case 4A

The shield loss is inacceptably large comparing with the other AC losses in superconductors and coil supports. Therefore, it is necessary to develop the way to seal the FRP vessel through non-metalic metrial.

(4) Total AC loss

The loss for each PF coil components are summed up as listed in Table X-2-4. The loss for case 4A is about three times as large as that for the other cases, since the magnetomotive force is large. The loss for the helium leak shields is ten times as large as that for the other components, and therefore should be reduced.

2.1.4 AC loss due to plasma disruption

The abruptly changing magnetic field caused by the plasma disruption can generate the AC loss in PF coils as well as TF coils and the vacuum chamber etc.

The loss can be obtained, according to the formulae listed in Table X-2-3. The loss averaged over the duration time is listed in Table X-2-5. It must be decreased if the shielding effect could be considered.

2.2 Forces and torques

In this section, the following structures are considered in view of the electromagnetic force during plasma disruption;

(1) first wall

(2) limiter plate

(3) blanket structure

(4) shield/vacuum vessel and bellows.

The electromagnetic interactions among these structures should be taken into account but these effects are neglected throughout the following analyses.

The evaluation method of the electromagnetic forces is based on Reference 1). In section 4 Methodology, the method will be describe briefly.

(1) First wall

The first wall has many grooves on its surface from the requirement of reducing the thermal stress. Therefore, the electromagnetic forces on its each section separated with grooves are small enough to withstand with its own stiffness. The most important effect of the force during the disruption is tearing the melted region from the surface.

The modes of electromagnetic forces are schematically shown in Table X-2-6. Judging from Table X-2-6, $(F_T)n$ (= $I_{eddy} \times B$ toroidal) will provide the serious problem with respect to the tearing. The parallel and normal components of magnetic field by plasma current along the first wall are summarized in Fig.X-2-4. The pressure exerting on the melted region P_{melt} is expressed by:

$$P_{melt} = \frac{d_{melt}}{d_{wall}} \times P$$

d_{melt} : thickness of the melted region

d_{wall} : thickness of the first wall

P : average pressure shown in Fig.X-2-5

When the melting occurs, the melted region will be lost into the plasma unless the surface tension is large relative to P_{melt}.

Torques due to $(F_t)_n$ and $(F_p)_n$ (See Table 1) are represented in Fig.X-2-6 and Fig.X-2-7. Stresses caused by these torques are far below the stainless steel allowable stress.

(2) Pump limiter

(a) Flat type

The pump limiter suffers the large electromagnetic force induced by the interaction between the eddy current and toroidal magnetic field, as depicted in Fig.X-2-8. In order to reduce the force in the copper cooling plate as much as possible, grooves are cut nearly up to the rear side of the copper plate. The torque and stress on the stainless steel reinforcement are shown in Fig.X-2-10 as a function of the limiter width.
The magnetic field normal to the pump limiter shown in Fig.X-2-9 is applied in calculating the results in Fig.X-2-10. The joint between the copper plate and reinforcement is subjected to the same shear stress as appears on the reinforcement. Hence, the width of about 170 mm in our design will be a reasonable selection.

(b) Double edge type

Eddy current is induced in the pump limiter during a plasma disruption. Electromagnetic force dur to the interaction between the eddy current I and toroidal magnetic field B_T is shown conceptually in Fig.X-2-11.

Consequently electromagnetic force causes torsion to the limiter.

Stainless steel type 316 is used for the reinforcement of the pump

limiter against the torques induced by the electromagnetic force. In order to reduce the force in the copper cooling plate as much as possible, grooves are cut nearly up to the rear side of the copper plate. Torque and stress on the stainless steel reinforcement for the double-edged limiter are shown in Fig.X-2-12 as a function of limiter width. The joint between the copper plate and reinforcement is subjected to about the same shear stress as appears on the reinforcement. The allowable stress is 0.8 Sm (Cu: 0.8 Sm = 31 MPa, stainless steel: 0.8 Sm = 108 MPa), according to the ASME Sec.III. Hence, the width of about 340 mm at R = 5 m is necessary to sustain electromagnetic force.

(3) Blanket structure

It is not easy to analyze the sophisticated blanket structure as a whole. The following assumptions are employed here for the preliminary study;

(a) Inner blanket and outer blanket are independently simplified with slab having equivalent thickness.

(b) The neutron shield structure in the inner blanket is divided into slim segments with insulations. Therefore, eddy current in the segments is small compared to that in the inner blanket structure.

(c) The lead neutron multiplier in the outer blanket is also divided into segments with insulations. However due to higher electrical conductivity of lead than that of stainless steel, the eddy current in the segmented multipliers is not negligible even if each volume of them is small.

Normal and parallel components of magnetic field should be taken into account as well as the case of the first wall. The patterns of electromagnetic force due to these two components are listed in Table X-2-7

together with calculation conditions. It should be noted that the outer blanket is subjected to the electromagnetic force in the lead neutron multiplier in addition to the forces listed in Table X-2-7.

Torque on the blanket structure are shown in Fig.X-2-13 and Fig.X-2-14. The toroidal magnetic field at the other blanket is lower than that at the inner blanket, but large volume of the outer blanket makes the electromagnetic forces severer.

The effects of the lead neutron multipliers on the electromagnetic forces can be understand from Fig.X-2-15. Comparing the results in Fig.X-2-15 with Fig.X-2-13 and Fig.X-2-14 the following matters are pointed out relating to the forces on the outer blanket;

(a) The lead neutron multiplier dominates the electromagnetic force due to parallel component of magnetic field.

(b) Meanwhile, the force due to normal component is mainly caused by the outer blanket itself.

The total torques are as follows;

- Inner blanket

  due to normal component 3.5×10^4 N-m

  due to parallel component 1.8×10^4 N-m

- Outer blanket (includes the effects of the multipliers)

  due to normal component 4.15×10^5 N-m

  due to parallel component 1.6×10^5 N-m

(4) Shield/Vacuum vessel and bellows

The shield consists of the rigid ring and bellows. It is possible to make the rigid ring strong to withstand the electromagnetic force, but the bellows is probably not allowed to be sufficiently stout since it has a role of keeping the loop resistance over 0.2 mΩ. The electromagnetic forces

exerting on the bellows are illustrated in Fig.X-2-16(b). As shown in Fig.X-2-16 the shear force F_T ($\equiv I_c \times B_T$) is inflicted on the bellows and the force F_p ($\equiv T_c \times B_p$) acts as the pressure.

About 1.6 MA of eddy current passes through the follows during the plasma disruption as shown in Fig.X-2-17. Table X-2-8 represents the electromagnetic forces F_T and F_p, and the model for this calculation. The subdivided elements in this model are regarded as the independent equivalent electrical circuits to set up the circuit equations.

The shear stress by F_T is roughly expressed by:

$$\tau = \frac{(F_T)_{total}}{H \times \ell} = 0.36 \text{ MPa}$$

$(F_T)_{total}$; total shear force of upper bellows (= 0.35 MN)

H ; height of bellows (= 80 mm)

ℓ ; peripheral length of upper bellows (= 12 m)

The average pressure P_{av} by F_p by also described by:

$$P_{av} = \frac{(F_p)_{total}}{H \times \ell} = 0.03 \text{ MPa}$$

These values are probably acceptable though the elaborate analyses are required.

The circulating eddy current I_c turns gradually into the saddle current I_s which brings about the tilting force F_t as shown in Fig.X-2-17. This force damages the joint part of the rigid ring and bellows provided that the rigid rings decline. If the assumption that all the circulating current turns into the raddle current is tentatively adopted here as the severest case, each of the rigid rings undergoes the torque of 2.5×10^7 N-m. This force should be taken into account in designing the shield structure.

2.3 Induced voltage on PF coils

Table X-2-9 to Table X-2-11 show the voltage on PF coils for normal operation. The voltage will be decreased below 10 kV by the introduction of parallel circuit, but the voltage level seems pretty high, judging from the current techniques. The most suitable overall system design would overcome this situation.

During plasma disruption, PF coils are exposed to the high induced voltages due to the change of plasma current. Assuming the low impedances of power supplies for PF coils, these induced voltages produce the induced currents in PF coils. PF coil currents under plasma disruption are shown in Table X-2-12 for a disruption time constant of 20 ms. The current changes in PF coils are small. So it is considered that there are no problems on the voltages of PF coils and DC power supplies.

Table X-2-1 AC loss formulae in TF coil superconductor

1. Hysteresis loss

$$Ph_{\perp} = \frac{2}{3\pi} Jc(B)d\dot{B}_{\perp} \qquad (w/m^3)$$

$$Ph_{/\!/} = \frac{1}{6} Jc(B)d\dot{B}_{/\!/} \qquad (w/m^3)$$

2. Eddy current loss

$$Pe_{\perp} = \frac{1}{12\rho} a^3 b\dot{B}_{\perp}^2 \qquad (w/m)$$

$$Pe_{/\!/} = \frac{1}{2\pi^2\rho} \frac{a^3b^3}{a^2+b^2}\dot{B}_{/\!/}^2 \qquad (w/m)$$

3. Coupling loss

$$Pc_{\perp} = \frac{1}{\rho_{\perp}} \left(\frac{\ell P}{2\pi}\right)^2 \dot{B}_{\perp}^2 \qquad (w/m^3)$$

where,

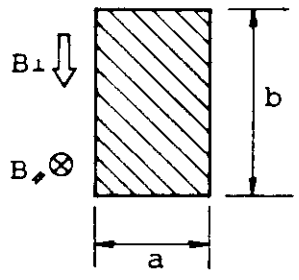

Cross section and field direction

Jc(B): critical current density

d : filament diameter

ρ : matrix resistivity

ρ : transverse resistivity

ℓP: twist pitch

Table X-2-2 AC losses in TF coils

	Case 1 (Pump limiter R=11m)	Case 2 (Pump limiter R=13m)	Case 4A (Divertor)
Superconductors	15.4 kW	14.5 kW	42.8 kW
Helium vessels	14.4 kW	14.1 kW	35.8 kW
Coil supports	26.2 kW	20.0 kW	70.5 kW
Sum	56.0 kW	48.6 kW	149.1 kW

Table X-2-3 AC loss formulae in PF coil superconductor

1. Hysteresis loss

$$Ph_{\perp} = \frac{2}{3\pi} Jc(B) d\dot{B}_{\perp} \qquad (w/m^3)$$

$$Ph_{\parallel} = \frac{1}{6} Jc(B) d\dot{B}_{\parallel} \qquad (w/m^3)$$

2. Eddy current loss

$$Pe_{\perp} = \frac{1}{4\rho} \dot{B}_{\perp} r_0^2 \qquad (w/m^3)$$

3. Coupling loss

$$Pc_{\perp} = \frac{1}{\rho_{\perp}} \left(\frac{\ell P}{2\pi}\right)^2 \dot{B}_{\perp}^2 \qquad (w/m^3)$$

where,

$Jc(B)$: critical current density

d : filament diameter

ρ : matrix resistivity

ρ : transverse resistivity

ℓP: twist pitch

γ_0: strand radius

Table X-2-4 AC losses in PF coils

	Case 1 Pump limiter R=11m	Case 2 Pump limiter R=13m	Case 3 (Divertor)
Superconductors	1.3 kW	1.4 kW	2.0 kW
Coil supports	2.5 kW	2.6 kW	10.4 kW
(Helium leak shields)	(20.3 kW)	(28.9 kW)	(43.0 kW)
Sum	3.8 kW (24.1 kW)*	4.0 kW (32.9 kW)*	12.4 kW (55.4 kW)*

* Taking account of the AC loss in helium leak shields.

Table X-2-5 AC losses due to plasma disruption

	Case 1 Pump limitter R=11 m	Case 2 Pump limitter R=13 mm	Case 3 Divertor
Superconductor	1.8 kW	1.8 kW	1.9 kW
Coil Support	4.3 kW	4.0 kW	5.8 kW
Sum	6.1 kW	5.8 kW	7.7 kW

Table X-2-6 Electromagnetic forces on the first wall and their effects
(the case of plasma disruption)

	Mode of electromagnetic force	Effects
Normal component of magnetic field by plasma current	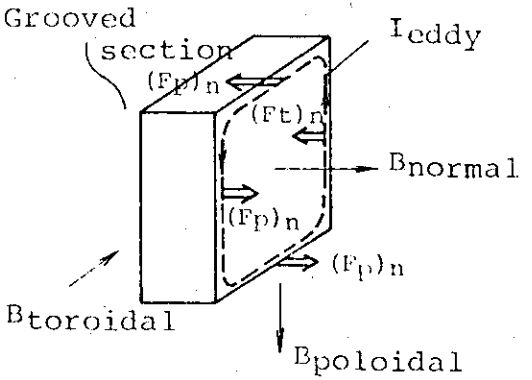 $(Ft)_n$: $I_{eddy} \times B_{toroidal}$ $(Ft)_n$: $I_{eddy} \times B_{poroidal}$	1 Each section separated with grooves is tensed or compressed by $(Ft)_n$ and $(Fp)_n$. 2 The melted region of the first wall will be lost into the plasma region.
Parallel component of magnetic field by plasma current	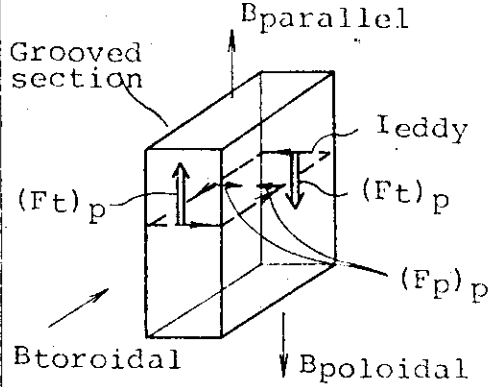 $(Ft)_p$: $I_{eddy} \times B_{toroidal}$ $(Ft)_p$: $I_{eddy} \times B_{poloidal}$	1 $(Ft)_p$ acts as the torsion on the each section separated with grooves. 2 The melted portion will not go into the plasma region as the direction of $(Fp)_p$ on the surface is converse.

Table X-2-7 Simplification of the blanket for calculation

	Inner blanket	Outer blanket (1)
Normal component of magnetic field by plasma current	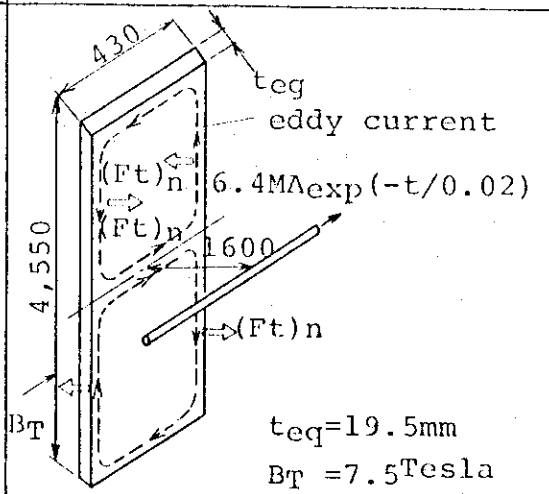	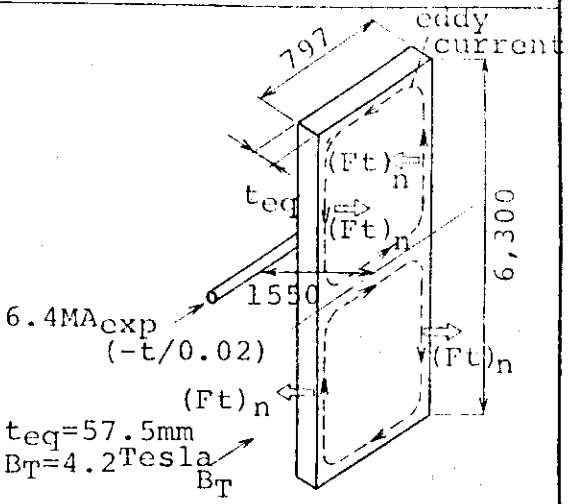
Parallel component of magnetic field by plasma current	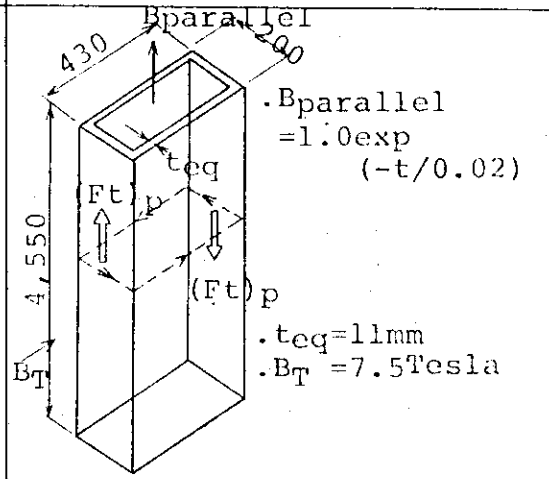	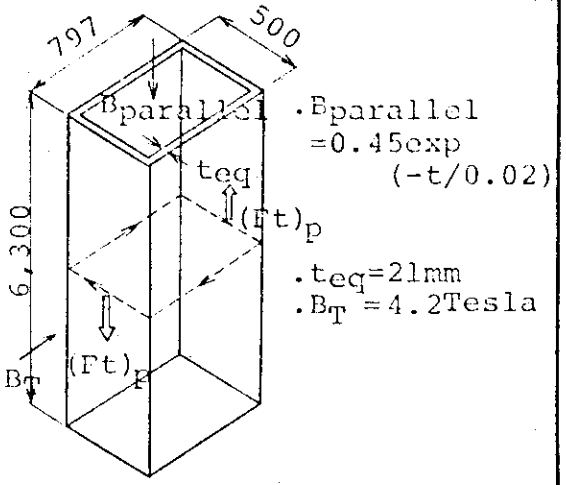

(1) The electr
magnetic for
in lead neut
multiplier a
added to the
forces.

Table X-2-8 Distribution of electromagnetic force in the bellows

EK No.	B_T	F_T	F_P
1	8.94 Tesla	50705 N	2832 N
2	8.94	42199	2362
3	8.94	31889	1784
4	8.06	24902	1548
5	6.22	28087	2254
6	5.1	27881	2734
7	4.35	25176	2891
8	3.69	20972	2842
9	3.69	26529	3597
10	3.69	32987	4469
11	3.69	37828	5125
Total	-	349155	32438

Notes: 1 Poloidal magnetic field Bp is assumed to be 0.5 Tesla.

2 Eddy current; values at 16 msec

3 Model

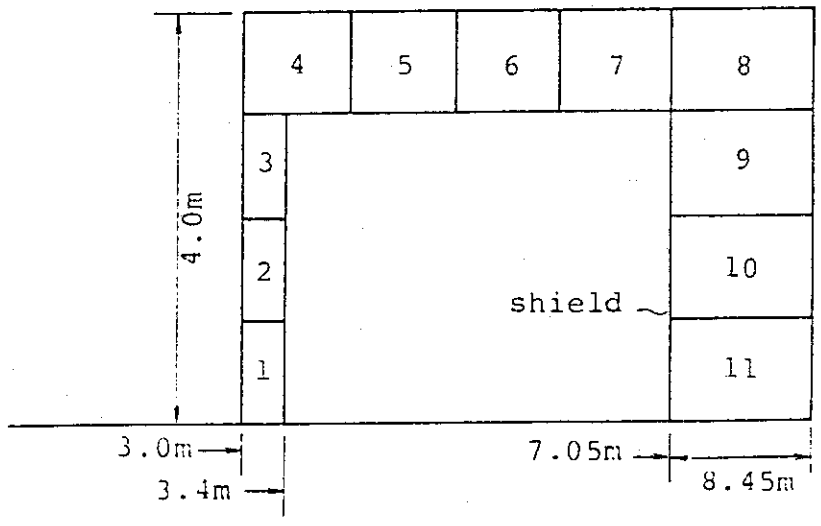

Table X-2-9 Voltage on PF coils (Case 1)

Unit: V

Coil No.	Block No.	Time					
		0S∿0.3S	0.3S∿5S	5S∿11S	11S∿211S	211S∿226S	226S∿246S
1	1	-1661.5	-724.7	-43.2	-3.1	153.4	124.1
2	2	-1629.9	-726.2	-46.3	-3.1	155.3	123.4
3	3	-1647.9	-726.1	-44.6	-3.1	154.4	123.9
4	4	-1665.7	-715.5	-40.0	-3.1	150.0	123.5
5	5	-1728.4	-694.6	-28.8	-3.1	140.1	123.6
6	6	-1855.2	-643.0	-4.0	-3.1	117.2	123.0
7,19	7	-4150.2	-1070.8	93.9	-6.1	136.8	244.1
8,9,11 20,21,23	8	-8799.6	-1947.9	256.0	-14.1	120.3	563.6
10	9	2743.6	194.4	-13.0	-6.9	-387.4	276.8
12	10	-14433.2	-6377.5	-3314.7	-7.0	3333.6	279.1
13	11	-1661.1	-724.1	-42.8	-3.1	153.1	124.1
14	12	-1629.5	-724.7	-45.1	-3.1	154.3	123.4
15	13	-1645.2	-722.3	-42.4	-3.1	152.2	123.9
16	14	-1662.6	-708.7	-36.2	-3.1	146.0	123.7
17	15	-1718.9	-682.5	-22.9	-3.1	133.5	123.9
18	16	-1854.3	-627.0	5.3	-3.1	107.3	124.1
22	17	7502.6	2640.4	843.7	-12.9	-1829.5	514.6
24	18	-15091.2	-7682.2	-4570.8	-8.8	4184.3	352.8

Note: *1) No.12 and No.24 coils are divided into 2 parallel current path and the resultant maximum voltages are below 10kV.

Table X-2-10 Voltsge on PF coils (Case 2)

Unit: V

Coil No.	Block No.	Time					
		0S∿0.3S	0.3S∿5S	5S∿11S	11S∿211S	211S∿226S	226S∿246S
1	1	-1670.1	-734.0	-56.9	-3.1	162.1	124.1
2	2	-1638.6	-735.6	-60.3	-3.1	164.1	123.3
3	3	-1656.4	-735.4	-58.4	-3.1	163.1	123.8
4	4	-1673.1	-724.4	-53.4	-3.1	158.4	123.4
5	5	-1734.2	-703.0	-41.0	-3.1	147.8	123.6
6	6	-1857.5	-650.4	-13.4	-3.1	123.4	123.0
7,19	7	-4136.7	-1080.1	81.6	-6.1	144.5	244.1
8,9,11 20,21,23	8	-8652.0	-1928.4	205.9	-14.1	131.8	563.1
10	9	3036.0	299.1	-160.8	-6.9	-366.6	276.5
12	10	-20837.3	-9088.8	-4608.4	-7.2	4818.2	289.6
13	11	-1669.2	-733.4	-56.6	-3.1	161.8	124.1
14	12	-1637.5	-733.7	-59.6	-3.1	163.1	123.4
15	13	-1652.3	-731.0	-57.1	-3.1	161.0	123.9
16	14	-1667.7	-716.7	-51.0	-3.1	154.6	123.7
17	15	-1721.1	-689.7	-37.2	-3.1	141.5	123.9
18	16	-1851.5	-632.7	-7.0	-3.1	114.0	124.1
22	17	8460.0	2935.2	284.1	-12.5	-1702.8	500.3
24	18	-22127.2	-11878.8	-6522.2	-9.5	6392.3	381.0

Note: *1) No.12 and No.24 are divided into 2 parallel current path and the resultant maximum voltages are below about 11kV.

Table X-2-11 Voltage on PF coils (Case 3)

Unit: V

Coil No.	Time					
	0S∿0.3S	0.3S∿5S	5S∿11S	11S∿211S	211S∿226S	226S∿246S
1	-1835.0	-686.7	-50.2	-3.1	149.4	122.9
2	-1611.1	-681.7	-46.3	-3.1	142.5	122.2
3	-1507.7	-632.6	-35.8	-3.1	120.3	122.7
4	-1440.8	-522.1	-15.8	-3.1	76.7	122.4
5	-1383.0	-460.7	1.2	-3.1	49.2	122.7
6	-1281.7	-422.2	23.6	-3.1	26.6	122.3
7	-1119.0	-398.2	52.1	-3.1	3.5	123.2
8	-986.4	-399.0	34.1	-2.9	16.6	114.8
9	-1322.0	-509.7	39.7	-3.5	33.1	137.5
10	-1372.5	-307.5	67.6	-2.0	17.3	79.7
11	-1796.7	-476.8	318.8	-2.0	-21.4	79.5
12	-245.8	-71.3	-48.4	-0.5	28.1	18.6
13	-1087.2	121.8	-2605.1	-3.3	893.8	132.2
14	-2378.2	-661.0	-52.6	-3.1	153.2	122.9
15	-2632.3	-647.2	-53.9	-3.1	155.2	122.2
16	-2709.3	-634.7	-53.1	-3.1	152.0	122.7
17	-2665.7	-610.3	-50.2	-3.1	142.6	122.3
18	-2498.1	-572.7	-44.1	-3.1	124.8	122.6
19	-2089.7	-502.1	-32.0	-3.1	89.9	122.3
20	-1358.9	-391.6	-11.5	-3.1	31.9	122.9
21	-853.0	-270.0	3.7	-2.9	-14.7	115.2
22	-388.4	14.8	39.9	-3.5	-150.2	137.8
23	8396.2	6662.5	828.5	-13.4	-3118.8	533.4
24	11990.8	9642.4	1065.0	-15.1	-4286.3	600.9
25	-222.8	-79.9	-14.8	-0.3	21.7	13.8
26	-61123.3	-31410.1	-4265.0	-16.6	12116.5	656.0

Note: *1) No.26 coil is divided into 6 parallel current path and the resultant maximum voltages are below 12kV.

Table X-2-12 PF coil current under plasma disruption

Coil No.	Block No.	Time				
		0.0S	0.02S	0.04S	0.1S	0.2S
1	1	-38.57	-34.26	-32.67	-31.79	-31.75
2	2	-38.57	-34.80	-33.42	-32.65	-32.61
3	3	-38.57	-35.01	-33.70	-32.97	-32.93
4	4	-38.57	-35.45	-34.30	-33.66	-33.63
5	5	-38.57	-36.05	-35.12	-34.61	-34.58
6	6	-38.57	-36.15	-35.25	-34.76	-34.74
7	7	0.	0.3784	0.5176	0.5946	0.5985
8,9,11, 20,21,23	8	0.	2.365	3.236	3.717	3.742
10	9	49.74	51.84	52.58	53.00	53.02
12	10	-50.27	-48.34	-47.63	-47.23	-47.21
13	11	-38.57	-34.41	-32.88	-32.03	-31.99
14	12	-38.57	-35.22	-33.98	-33.30	-33.26
15	13	-38.57	-35.58	-34.47	-33.87	-33.83
16	14	-38.57	-36.10	-35.20	-34.70	-34.67
17	15	-38.57	-36.60	-35.87	-35.47	-35.45
18	16	-38.57	-37.13	-36.60	-36.31	-36.29
22	17	50.32	51.16	51.47	51.65	51.65
24	18	-49.29	-47.54	-46.89	-46.53	-46.52

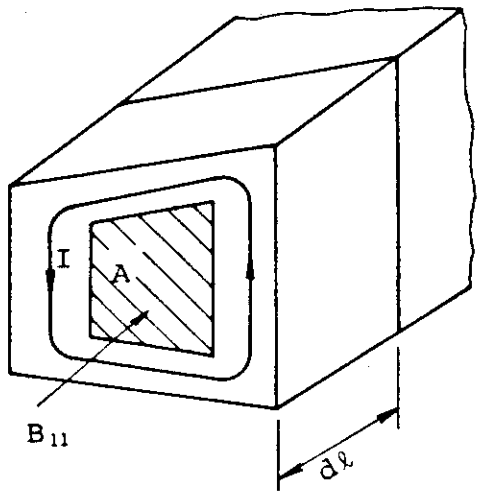

$$P_{\perp} = \frac{A_2}{\langle R \rangle} \int_{\ell} \dot{B}_{\perp}^2 \, d\ell$$

A : Crosssectional area

$\langle R \rangle$: Averaged resistance per unit length

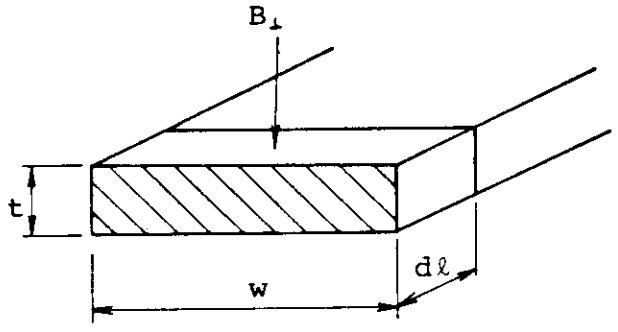

$$P_{\perp} = \frac{tw^3}{12\rho} \int_{\ell} \dot{B}_{\perp}^2 \, d\ell$$

t : Thickness

w : Width

ρ : Resistivity

Fig. X-2-1 The models for calculation of AC loss in TF vessel

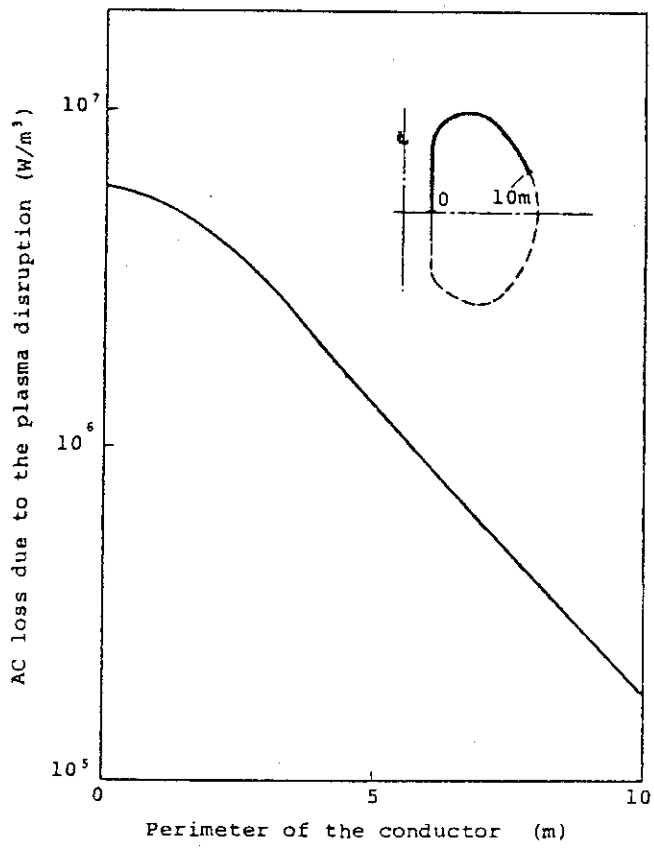

Fig. X-2-2 AC loss distribution along the superconductor

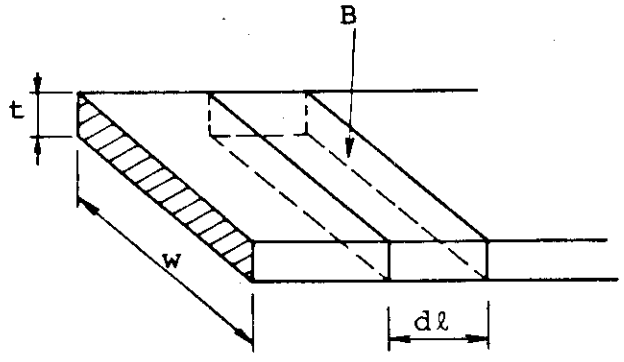

Fig. X-2-3 AC loss model

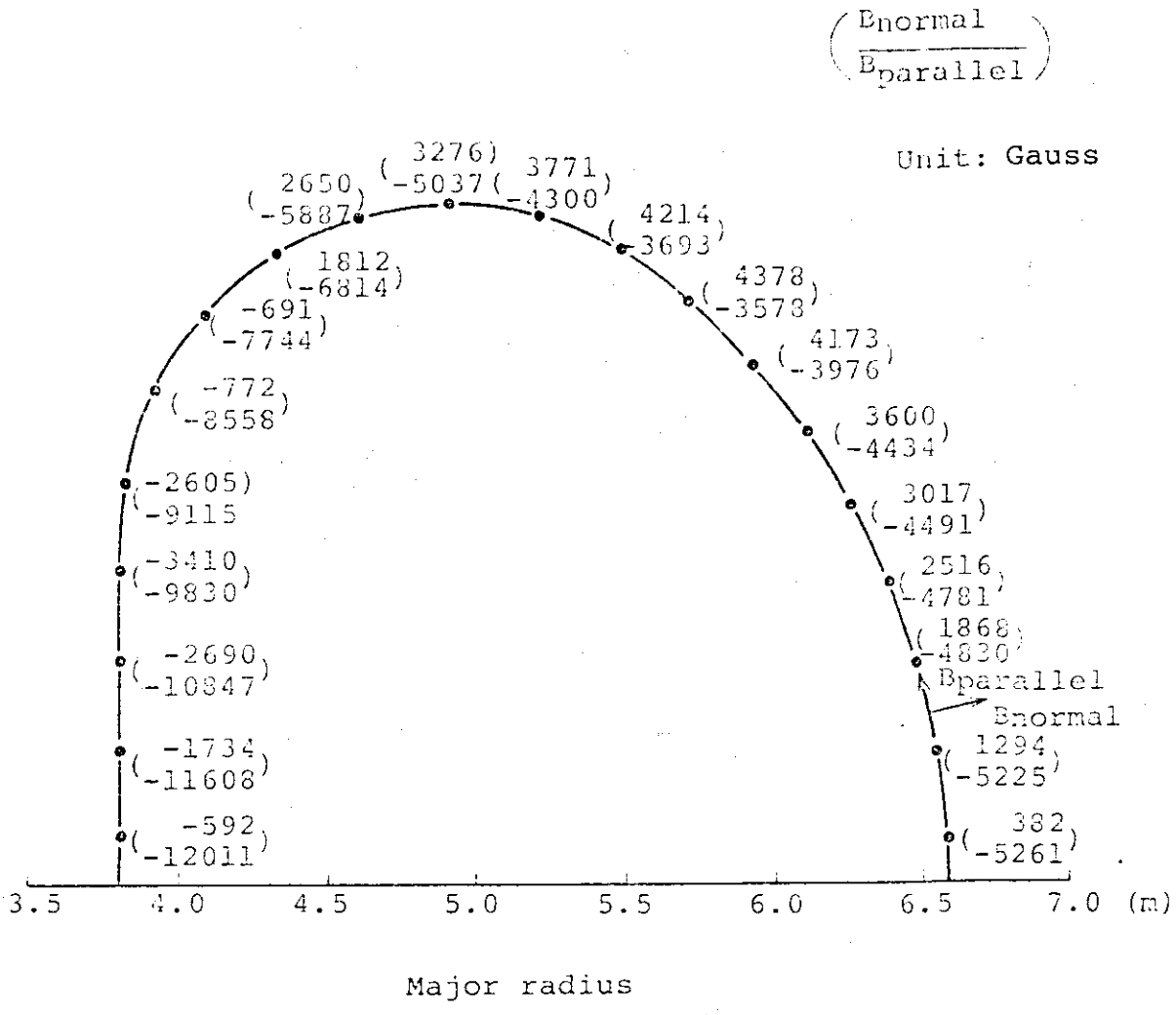

Fig. X-2-4 Magnetic field distribution along the first wall

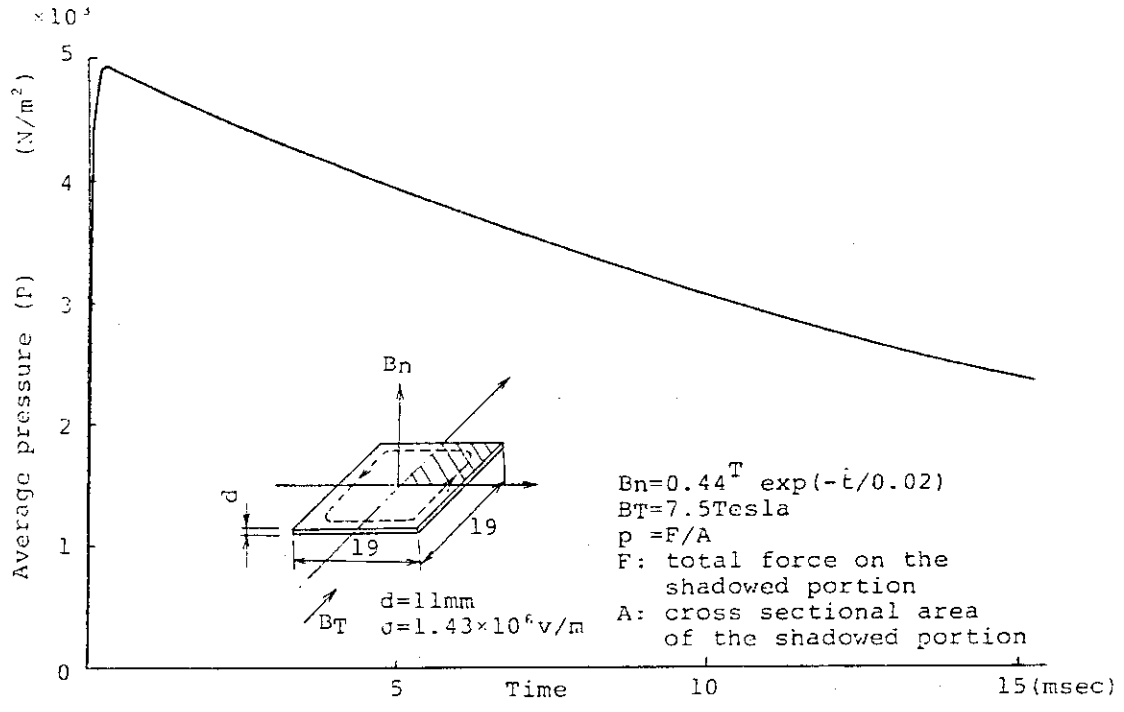

Fig. X-2-5 Electromagnetic force on the first wall (1)

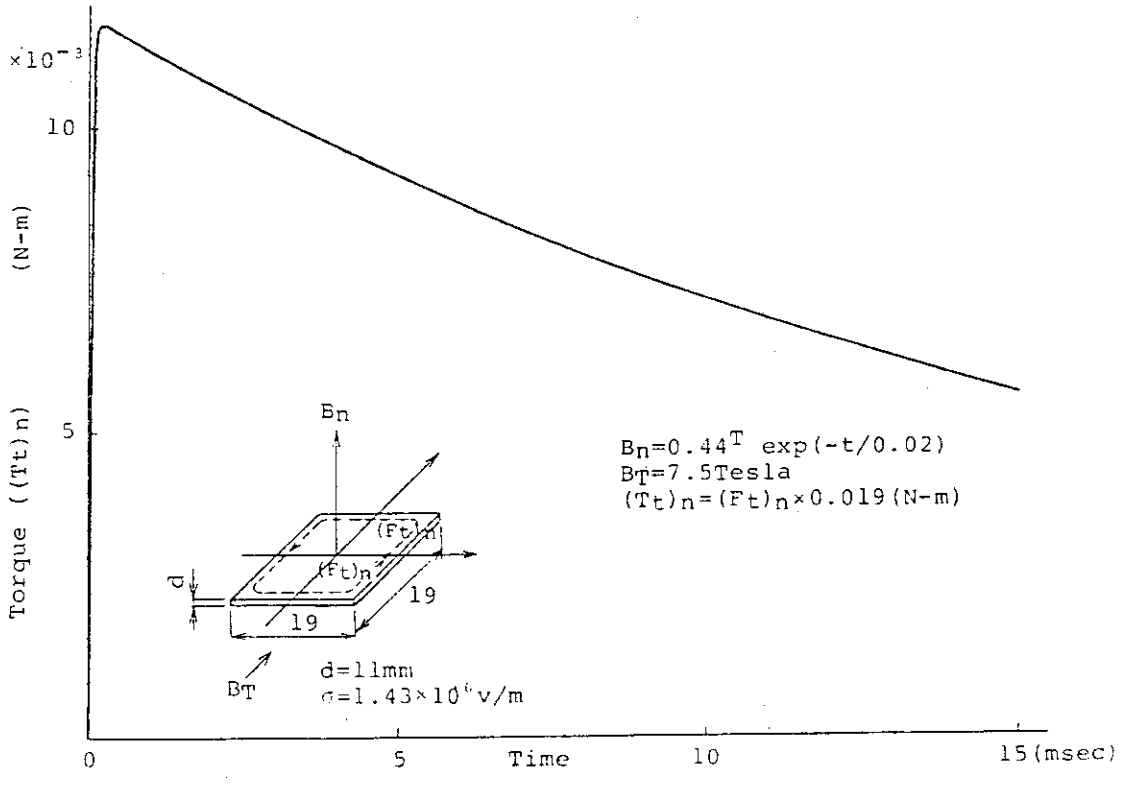

Fig. X-2-6 Electromagnetic force on the first wall (2)

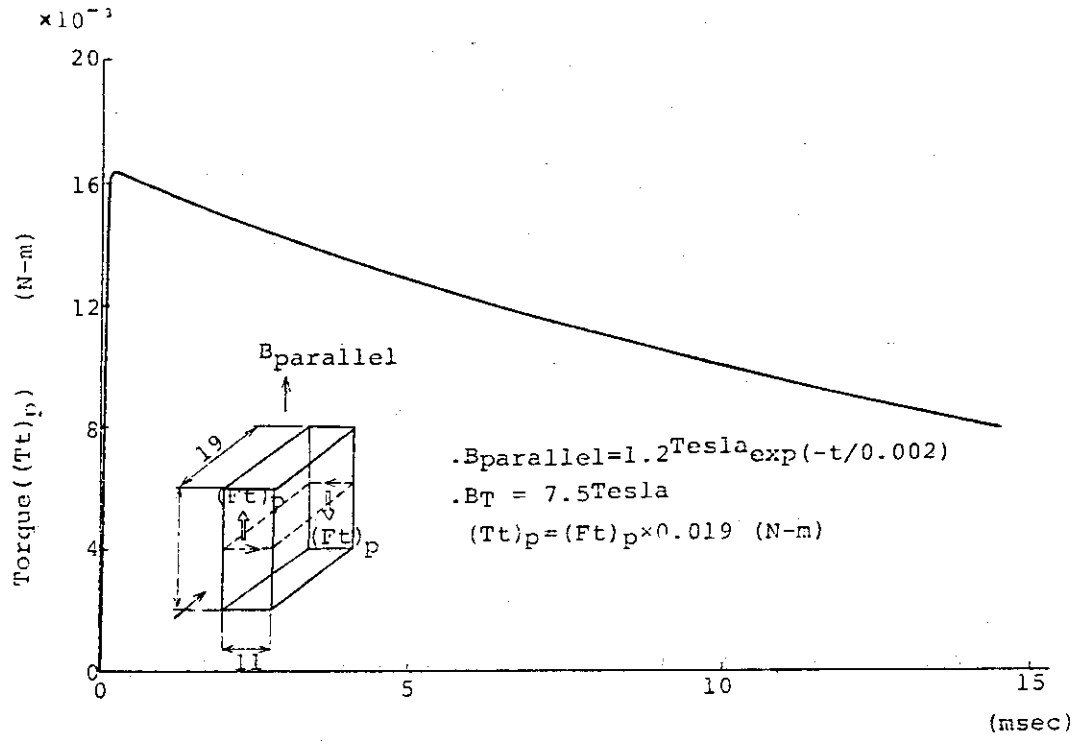

Fig. X-2-7 Electromagnetic force on the first wall (3)

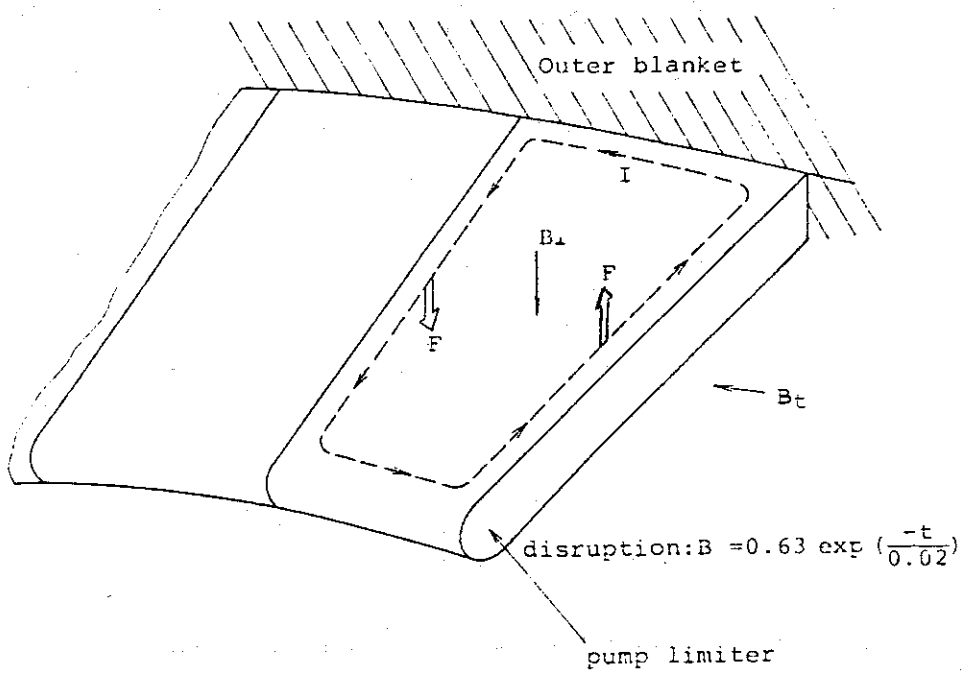

Fig. X-2-8 Model of electromagnetic force on the pump limter by eddy current

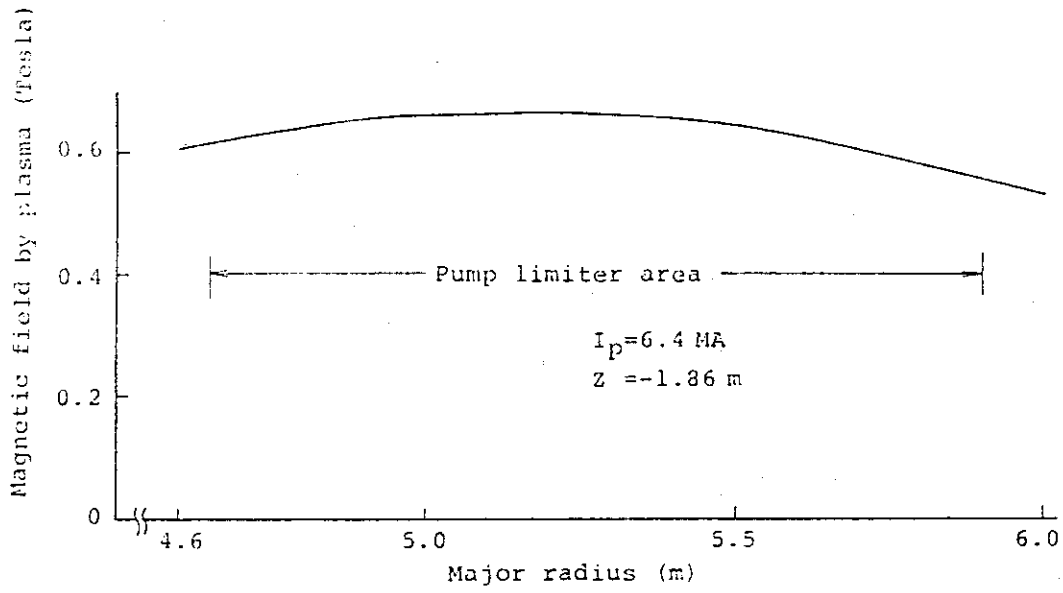

Fig. X-2-9 Magnetic field distribution normal to the pump limter

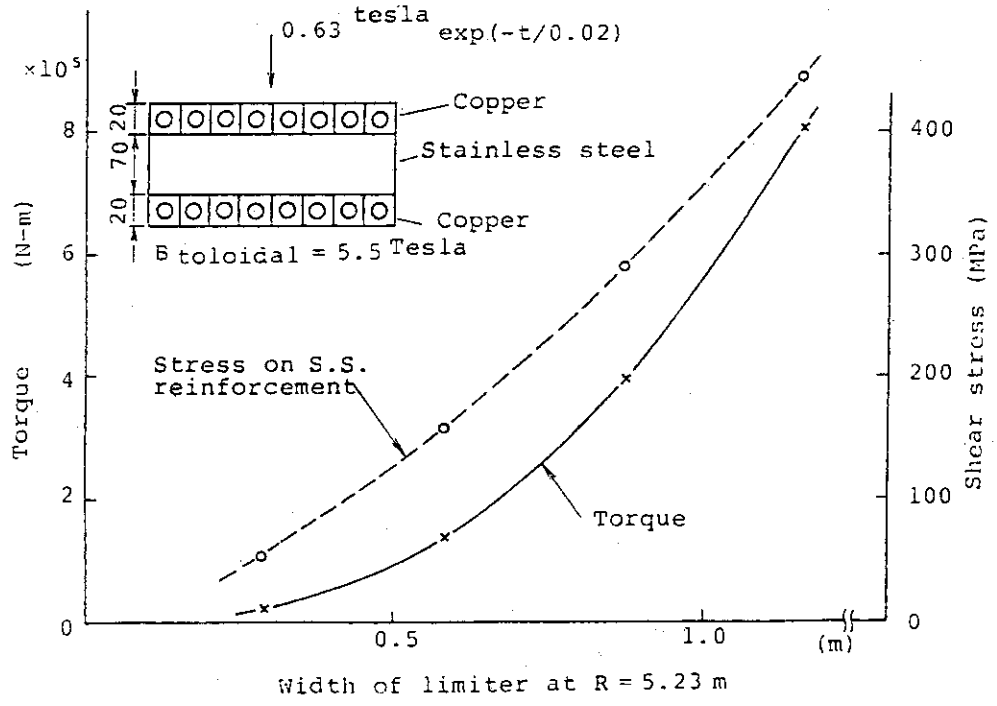

Fig. X-2-10 Electromagnetic force on the pump limter

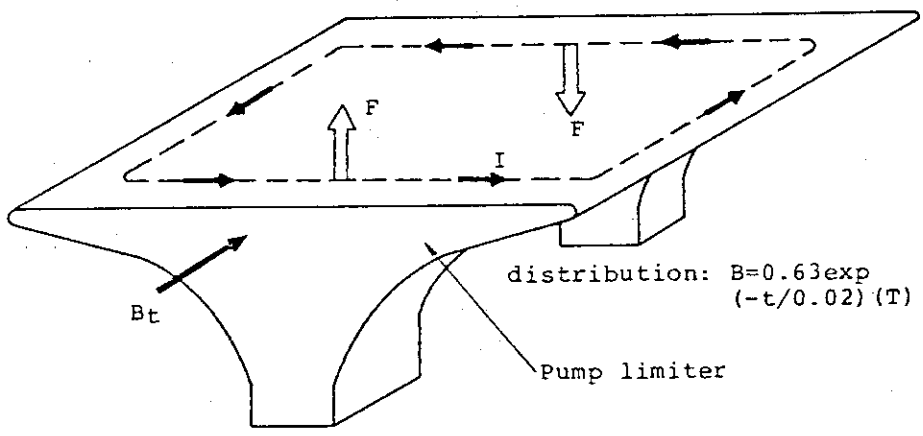

Fig. X-2-11 Model of electromagnetic force on the double edge pump limter by eddy current

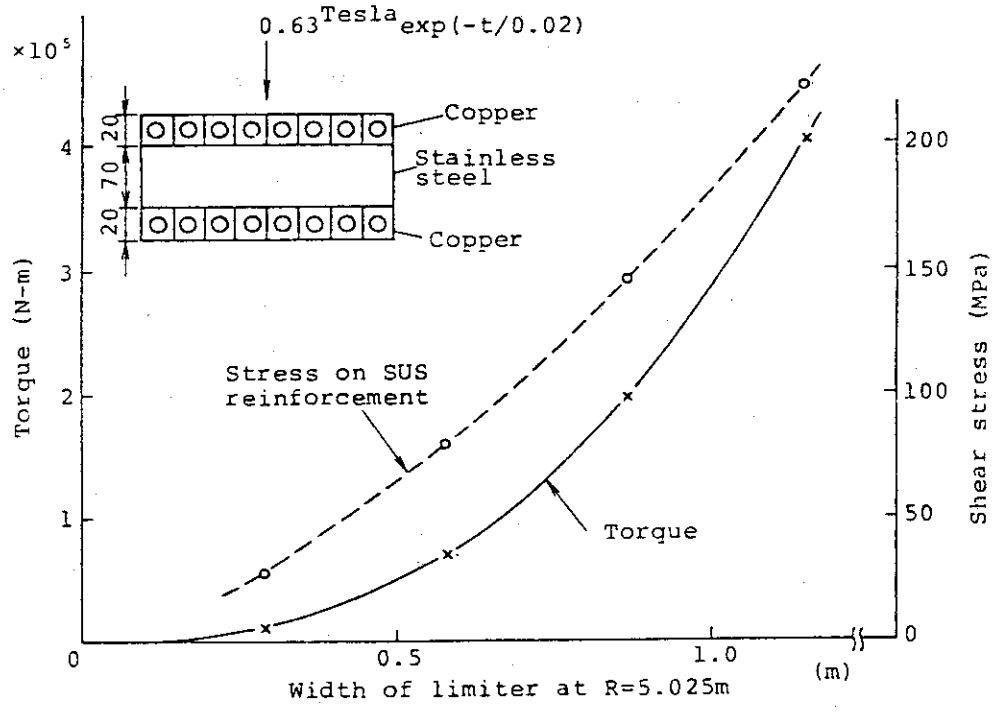

Fig. X-2-12 Electromagnetic force on the double edge pump limter

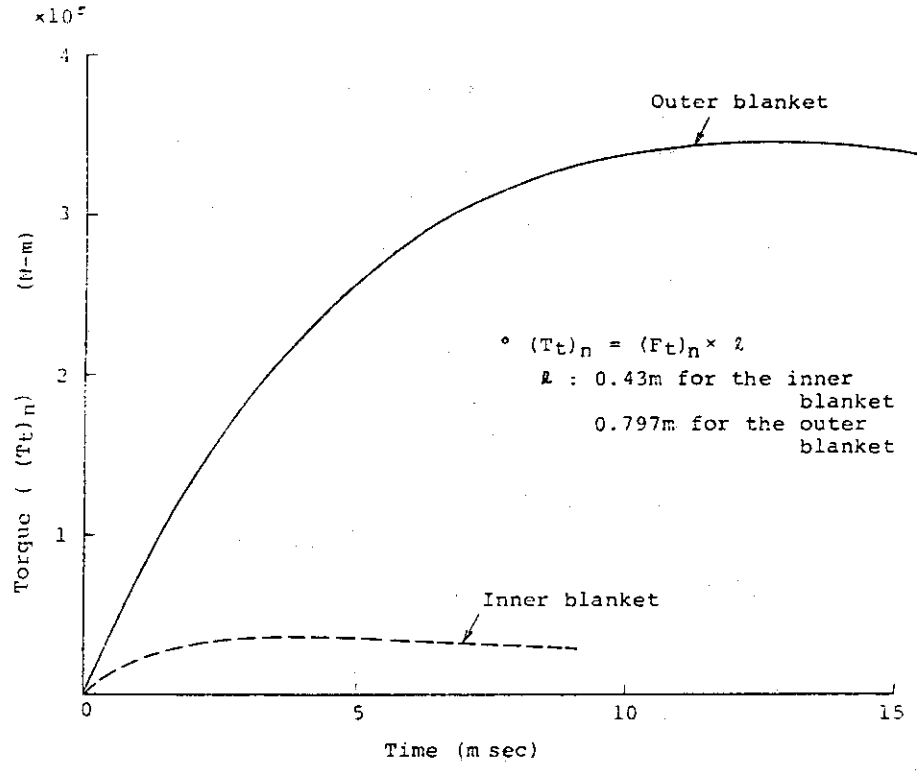

Fig. X-2-13 Electromagnetic force on the blanket due to normal component of magnetic field

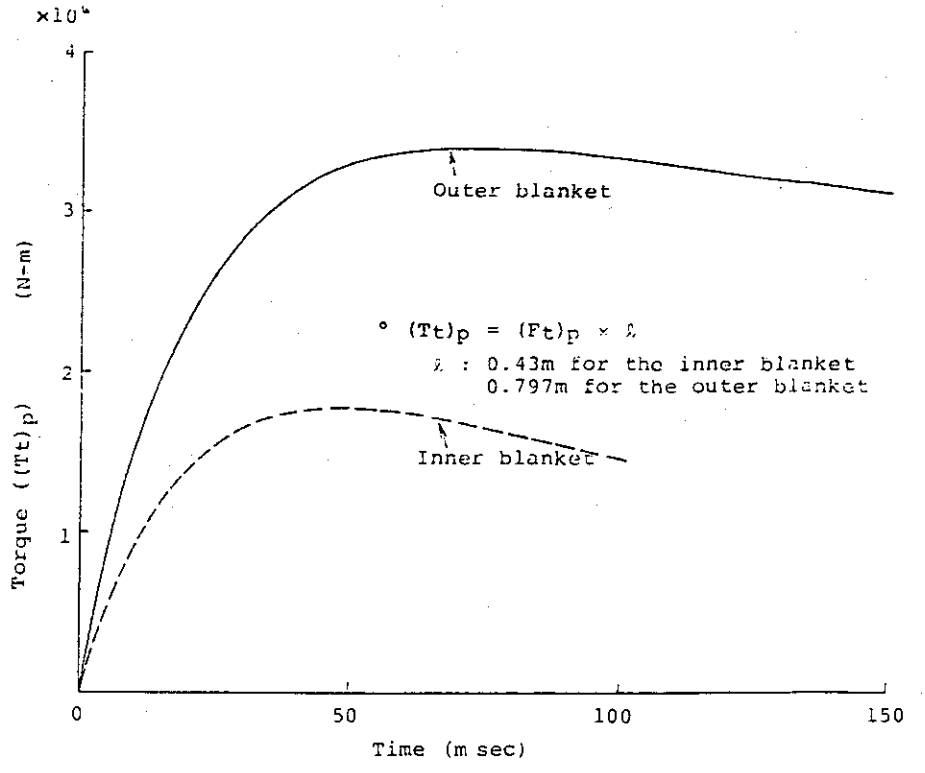

Fig. X-2-14 Electromagnetic force on the blanket due to parallel component of magnetic field

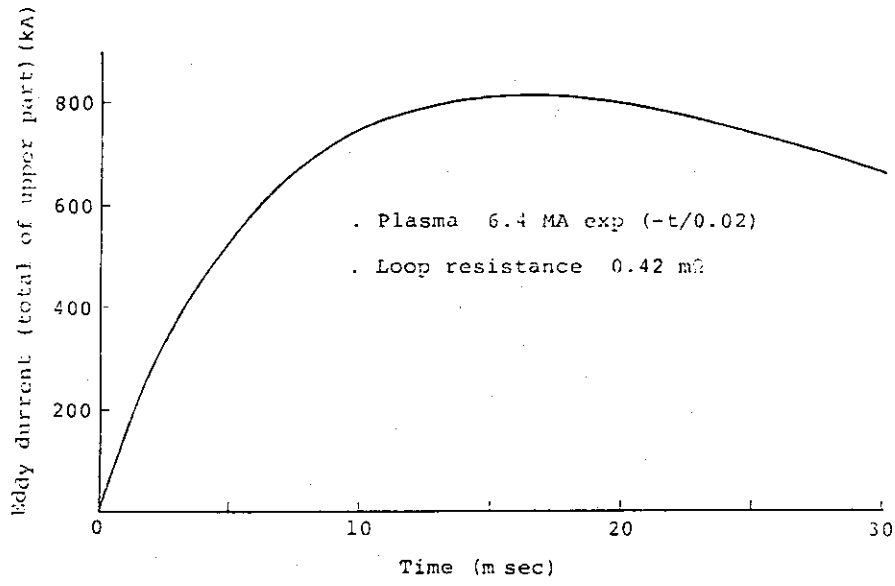

Fig. X-2-15 Eddy current in the bellows during plasma disruption

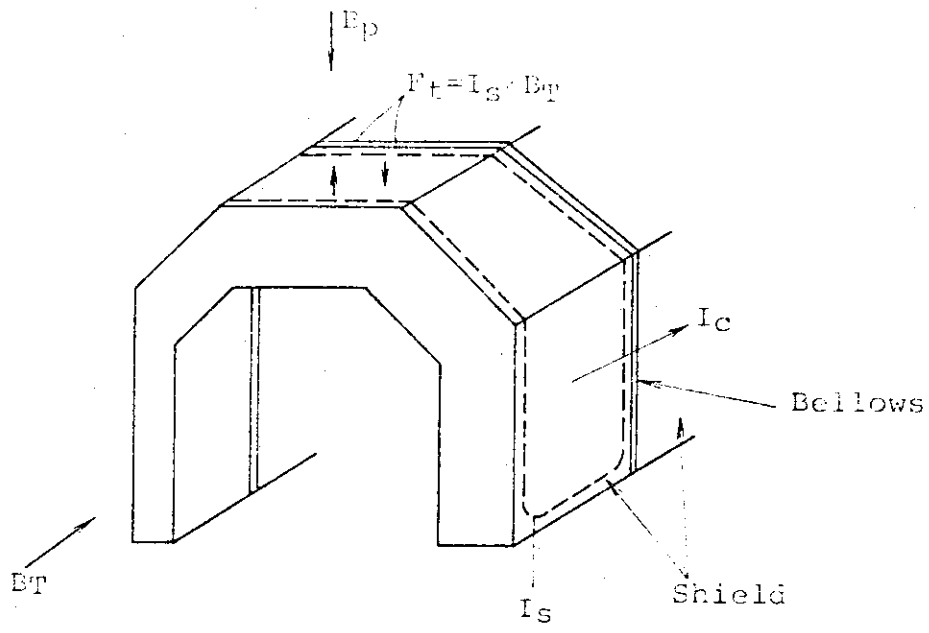

(a) rigid ring part

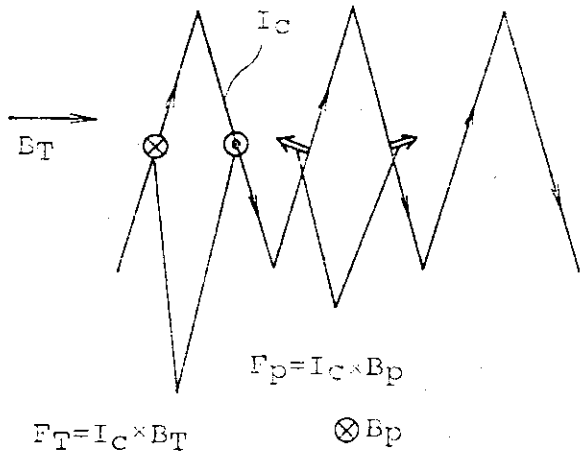

(b) bellows part

Ic: circulating current through bellows

I_S: saddle current

B_T: toroidal magnetic field

B_p: poloidal magnetic field

Fig. X-2-16 Electromagnetic forces in the shield

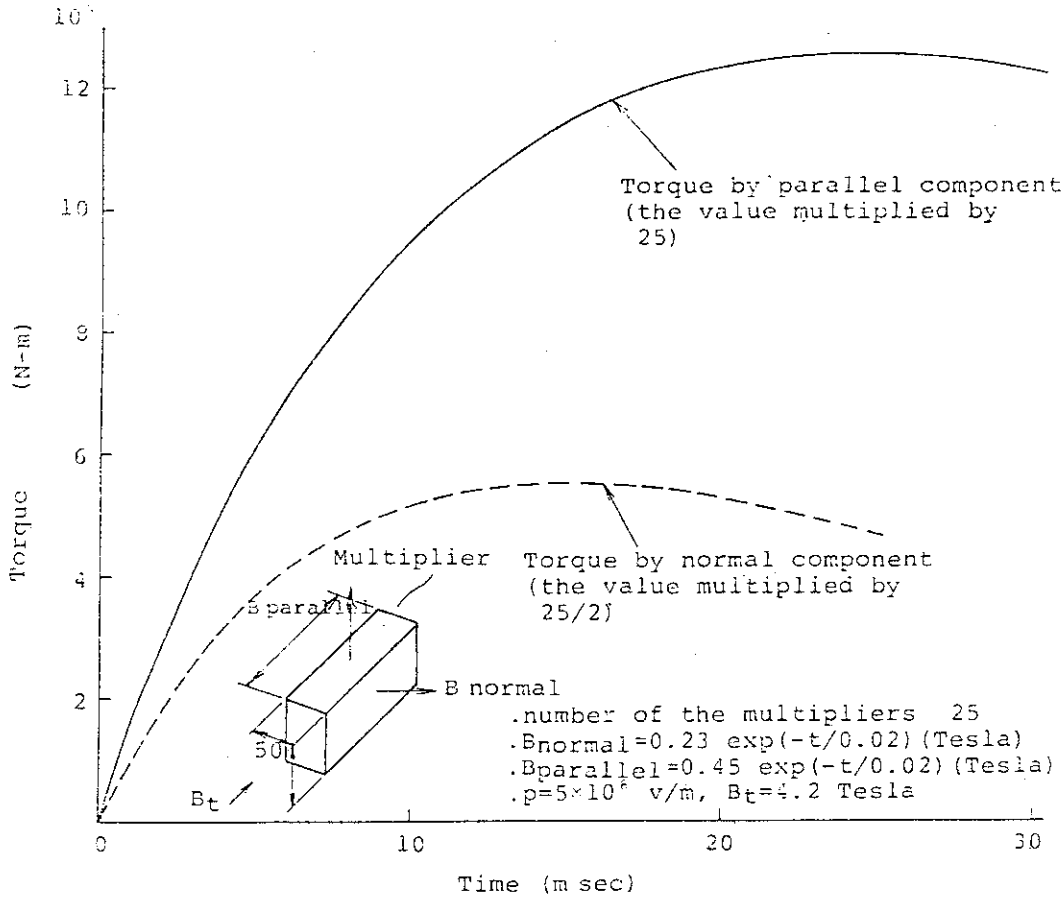

Fig. X-2-17 Electromagnetic forces in the lead neutron multiplier due to normal and parallel magnetic fields

3. Passive Stabilization

The shell effect of induced currents upon the plasma positional control must be evaluated from the viewpoint of both a positive function as the passive stabilization (so-called shell effect) and a negative function which is an obstruction to field penetration by active control. A seriese of the shell effect studies was presented on INTOR Workshops throughout the Phase I and the Phase II-A[2),[A1] A comprehensive study is described in Reference [A1].

3.1 Vertical

The passive shell effect is indispensable for quick suppression of the vertical position instability in order to save the power supply for active control. On INTOR specification for the passive shell effect, the shell structure has to suppress the plasma growth rate less than 20 sec^{-1}. The shell structure must be considered from the viewpoints of engineering feasibility (maintenability) and high tritium breeding ratio. Some candidates of shell structure are toroidally divided into 24 sectors to make the remote assembly and maintenance of the torus components. On this meaning, some structure concepts which are not divided in toroidal direction seem to be nonsense practically. But it is very useful to study these concepts for finding what type of shell structure is preferable.

3.1.1 Basic equations

An evaluation of shell effect is based on analyzing the interaction of a plasma column with a crowd of passively inductive structures surrounding the plasma column.

Plasma motion can be described by the following equation in the

sylindrical coordinates[3].

$$m_p \ddot{Z}_p = I_p \, (B_0 \cdot n/R_p) \cdot Z_p - I_p \, (\sum_{i=1}^{N} B_i + B_d) \qquad 3.1 \text{ —— } ①$$

And the relationship between the plasma column and the inductive structures can be expressed by the following circuit equation.

$$\dot{I}_i + \sum_{\substack{j=1 \\ (j \neq i)}}^{N} (M_{ij}/L_i) \cdot \dot{I}_j + (R_i/L_i) \cdot I_i$$

$$= - I_p \cdot [(\partial M_{pi}/\partial Z)/L_i] \cdot \dot{Z}_p \qquad 3.1 \text{ —— } ②$$

Here, Z_p, m_p, I_p and R_p are the axial displacement, mass per unit length, current and major radius of the plasma column respectively. B_0 and n are the axial component and n-index of the equilibrium field (Shafranov's field) at (R_p, 0.0), respectively. The subscript i means the i-th inductive structure. L, R and M are self-inductance, resistance and mutual inductance respectively. B_i and B_d are the radial component of the magnetic field produced at (R_p, 0.0) by I_i and a disturbance field, respectively. Moreover, B_i is expressed by the following equation.

$$B_i = \nu_i \cdot I_i \qquad 3.1 \text{ —— } ③$$

where ν_i is the radial field component per unit current at (R_p, 0.0).

The above inductive structures indicate the passive coils, a vacuum chamber, blankets, shield blocks and so forth. Various kind of inductive currents components on each structure can be expressed by eigen modal currents which are not coupled mutually. In this case, equations from Laplace transformation of Eq.3.1-① and Eq.3.1-② on using Eq.3.1-③ and setting 0.0 on B_d, give the following equation.

$$\tau_0^2 \cdot \gamma_g^2 = -[n + \sum_{m=1}^{M} \{n_m \cdot \tau_m \cdot \gamma_g / (1 + \tau_m \gamma_g\}] \qquad 3.1 \text{ —— } ④$$

where τ_0 is the intrinsic time constant of plasma column ($\equiv \sqrt{-m_p \cdot R_p / I_p \cdot B_0}$, $I_p > 0$, $B_0 > 0$), and γ_g and τ_m are the growth rate of the plasma vertical displacement and time constant of m-th modal current, respectively. $n_m (> 0)$ can be defined by the following equation.

$$n_m = \nu_m \cdot [(\partial M_{pm}/\partial Z)/L_m] \cdot (R_p I_p / B_0) \qquad 3.1 \text{ —— } ⑤$$

It can be said that if $\tau_m \cdot \gamma_g \gg 1$ and $(n + \sum_{m=1}^{M} n_m) > 0$, the shell effect can be expected for passive stabilization and on the other hand, if $\tau_m \cdot \gamma_g \ll 1$, no shell effect can be expected.

3.1.2 Studies of shell structure

The typical plasma parameters of INTOR are shown in Table X-3-1. The decay index (so-called n-index) is set os as to have -1.30 for the divertor plasma and -1.0 for the pump limiter plasma. Then it can be said that the shell effect is required much more for divertor plasma than the pump limiter plasma.

Analysis of the shell effect consist of the following process.

Step 1 —— The eddy current evaluation, in which the modal current analysis based on the finite element circuit method is used. The eigen modes of currents induced on shell structures can be calculated by higher order on using the same model. Here, only the largest eigen mode of those time constants is preliminary used on evaluating the positional stability.

Step 2 —— Evaluation of the derivative of its mutual inductance with the plasma column, $(\partial M_{ps}/\partial Z)$ (subscript "s" is used for the largest of those time constants), which is performed by both means of the dipole current model and a method by

using the plasma equilibrium codes.

The structural view nearby the plasma column is shown in Fig.X-3-1. The contour I is located exactly upon the first wall and the contour II is located between the blanket and the shield blocks.

[I] Shell structure on the contour I

It is useful to find out what shape of the shell structure is preferable in obtaining the large shell effect. Four kinds of shell structures shown in Fig.X-3-3 were investigated.

(a) Doughnut without cuts

This is the ideal shell-structure which surrounds the plasma column, and has the best performance as the shell.

(b) Doughnut with cuts

The doughnut-like shell is devided into 24 sectors in toroidal direction. Each sector is completely insulated or connected by bellows. This has the best shell performance among the shell-structures with cuts.

(c) Plane ring with and without cuts

The shell-structure consists of a plane ring surrounding the outboard side of the plasma column.

(d) Rectangular coils

Twenty-four coils are installed on the outboard side along the circuits which would carry the first eigen mode of the doughtnut with cuts. This would be the most preferable with respect to the breeding ratio and the assembly and maintenance of the device, if this shell-structure could has the sufficient shell effect. Each n_s for these shell structure concepts listed in Table X-3-3.

The ideal shell-structure of the case (a) perhaps gives the maximum n_s, which is obtained from the structure of INTOR, and, as a matter of course, is expected to have the adequate shell effect. The plane ring

without cuts placed only on the outboard, which is called (c'), is also expected to provide the well shell effect like as the case (a).

On the contrary, the shell-structures with cuts have the poor shell effect. Even though the shell-structures with cuts, that is, the cases (b) and (b') completely surround the plasma column, which is expected to be the best performance among those with cuts, n_s becomes less than one, and the insufficient shell effect can be provided. This poor shell effect of the shell-structures will be attributed to the fact that the first eigen mode of the induced current changes from the current in the toroidal direction to the saddle-type current.

Judging from the results in Table II, the shell-structures with cuts seem to be unsuitable for the sufficient shell effect.

In the above, the time constant of the shell-structure, τ_s has not been discussed. In the tokamak devices in which plasma currents are induced by means of the current transformer, there is the lower limit in the loop resistance, e.g., a few tenth mΩ. In this meaning, there is found to be the upper limit in τ_s.

The shell-structure with rings, which are shown in Fig.X-3-4 will be discussed in the followings. Some difficulties in the assembly and maintenance of the torus are accompanied with them. However some improvements can be expected in the breeding efficiency.

The results of the typical cases are in Table X-3-4. All cases have $n_s > 1$ and moderately decreasing shell effect from the case (a) to the case (f) is found to be anticipated.

As known in Table X-3-1, the decay indexes, n for the divertor and pump limiter are about -1.30 and -1.0, respectively. Therefore, as far as on attaching important to the breeding ratio, the shell structure shown in Fig.X-3-4 will perhaps give only the unsufficient shell effect for the

divertor, and then, its studies for the divertor will be performed on taking the contour I and II shown in Fig.X-3-1 into account simultaneously.

Prior to those studies, the cases (e) and (f) are investigated from the viewpoint of increasing the breeding efficiency in more detail.

The results of the case (e) and (f) are shown in Fig.X-3-5 and Table X-3-4. The figure shows the loop resistances, R_s, and τ_s versus the thickness of the ring plate, t, with a parameter of the width of the ring plate, L. Since the growth time of the positional instability depends on both of τ_s and n_s of the induced current, the total indicates that the longer τ_s does not always suppress the vertical motion of the plasma column during the longer time span.

The case (f.1.3) can stably maintain the plasma column almost during the same time time span as the case (e.1.1). When the blanket on the inboard side is non-breeding type, the case (e.1.1) is more preferable than the case (f.1.3).

In the above descriptions, the shell structures from the following points of view have been discussed.

(1) Doughnut-like shells with and without cuts, and rectangular coils as a special case of its shell with cuts.

(2) The shell-structure with some rings which are located on the contour I, and go around in the toroidal direction.

In the case (1), discrepancy in n_s between "without cuts" and "with cuts" except the rectangular coils is found to be remarkably large. This comes from increase of L_s, and decrease of $(\partial M_{ps}/\partial Z)$ and ν_s due to the change of toroidal mode current to saddle-like current. On the other hand, the case of the rectangular coils have the special feature that L_s is about 2.5 times more than on the plane ring without cuts and both of $(\partial M_{ps}/\partial Z)$ and ν_s is only a little less than on it. That is, the decrease

on both of $(\partial M_{ps}/\partial Z)$ and ν_s in the cases, "with cuts" is due to decrease of the toroidal component of eigen mode current, and this can be understood from the above result with the rectangular shell.

On the other hand, the case (f.1.3) in the above case (2) have the special feature that L_s is about 1.7 times more than on the plane ring without cuts and both of $(\partial M_{ps}/\partial Z)$ and ν_s are about 1.5 times more than on the doughnut-like shell without cuts.

Therefore it is clear that the above difference in L_s between the rectangular shell and the case (f.1.3) will be produced by two poloidal bars which constitute the two sides of a rectangular shell from the top over bottom of the torus. Also the difference in both of $(\partial M_{ps}/\partial Z)$ and ν_s among the case (f.1.3) and the doughnut-like shell without cuts will be produced by localizing the broad toroidal current on the doughnut-like shell upon the shell in the case (f.1.3) usefully.

In Fig.X-3-6 is shown dependence of $(\partial M_{ps}/\partial Z)$ upon the location of filament current along the contour I, obtained from the equilibrium codes. The shell in the case (f.1.3) is located nearly from No.8 over No.11 in the number of filament coil position in the figure. Its location of the case (f.1.3) is found to be near the optnum region.

One of 24 rectangular shells obtained on the basis of the above results is shown in Fig.X-3-7. The rectangular shell is at first presented on the INTOR Phase II-A Workshop Session V from the JAERI team. In Japan this shell has been presented as one of shell structures for the FER (SPTR)[6].

Together in the figure is given its dimension, too, and it has about 1.0 cm (τ_s = 126 msec) in uniform thickness of copper. It will be found to have a special feature that two poloidal bars bridged from the top over bottom of the torus has about 0.5 m in width of the radial direction.

This 24 rectangular shells has almost the same in n_s as with (f.1.3)

in Table X-3-4 but can have the desirable τ_s by selecting a appropriate value in its thickness.

But, two toroidal bars at its top and bottom, which have about 1 m in width of the poloidal direction, will have to be kept in its thickness as thin as possible because of making the breeding ratio more preferable.

From both of the purposes to obtain its thinner toroidal bars and to produce more effective shell effect for the divertor, it is necessary to study some shell structures located on the contour II.

[II] Shell structure on the contour II

Fig.X-3-8 shows four kinds of shell-structures located on the contour II. All kind of the shell-structures are constituted so as to be devided into 24 sectors in toroidal direction, and each of the sectors on those shell-structures have two poloidal bars (side plates) such as in Fig.X-3-7.

Fig.X-3-8(a) is in the case which surrounds the plasma column completely, and will give the best shell effect among those in Fig.X-3-8. n_B which is shown together in the figure is n_1 (for the largest time constant of its eigen mode) on Eq.3-1 —⑤ corresponding to n_s in the above Section.

n_B for Fig.X-3-8(a), (b), (c) and (d) is found to have about 1.71, 1.20, 1.05 and 1.13, respectively. Therefore, (d) similar to (f.1.3) in Table X-3-4 should be selected as better shell-structure lacated on the contour II because (a) and (b) can not be used on taking the access area of the divertor or pumplimiter into account.

Table X-3-5 shows each growth time (which is a reciprocal of growth rate) of the plasma column from the shell-structures located simultaneously on both of the contour I and II. These shell-structures consist of the case of (f.1.3) on contour I and the case in Fig.X-3-8(d).

The mutual inductance between these structures is set so as to have about 10 μH. It is found that the case of 25 msec in τ_s will produce its growth rate less than and equal to (1/50) ($msec^{-1}$) on selection of τ_B more than 250 msec. 25 msec in τ_s is equivalent to about 2.6 mm in thickness of the toroidal bars. If these cases, 250 or 500 msec in τ_B cannot give the stable control of the vertical positional motion, any cases more than 50 msec in τ_s will have to be selected for parameters of the shell-structures.
In such a case, the influence of the thickness of toroidal bars upon the bleeding ratio cannot be perhaps ignored.

3.2 Radial

The equilibrium field whose n-index is negative value does not always cause the radial displacement of a plasma column. However the radial displacement can be caused by the change of the plasma beta poloidal or by the change of the plasma internal inductance. The plasma beta poloidal can be changed by the auxiliary heating and the plasma internal inductance can be changed by the change of plasma current profile.

The calculation of the induced currents on the torus structures by the plasma radial displacement can employ the same method with the vertical displacement.

Table X-3-1 Major Parameters of the INTOR

Major Radius , R_p (m)	5.3
Minor Radius , a_p (m)	1.2
Plasma Current , I_p (MA)	6.4
Divertor Plasma	
Elongation , K	1.6
Shafranof's Field , B_0 (T)	- 0.50
Decay Index , n	- 1.30
Pump Limiter	
Elongation , K	1.5
Shafranof's Field , B_0 (T)	- 0.52
Decay Index , n	- 1.0

Table X-3-2 Decay Index for Shell-structure in Fig.X-3-3

Cases	n_s
(a) Doughnut without cuts	2.35
(b) Doughnut with bellows	0.73
(b́) Doughnut with cuts	0.75
(c) Plane ring with cuts	0.73
(ć) Plane ring without cuts	2.25
(d) Rectangular coils	0.64

Table X-3-3 Decay Index for Shell-structure in Fig. X-3-4

Cases	(a)	(b)	(c)	(d)	(e)	(f)
n_s	2.35	2.32	1.96	2.32	1.82	1.52

Table X-3-4 Shell Effect with Shell-structures for Cases (e) and (f) in Fig. X-3-4

Cases	R(mΩ)	L_1	L_2	τ_s(ms)	n_s	γ_g^{-1}(ms)
(e.1.1)	0.25	0.44	0.64	24	1.53	22
(e.1.2)		0.73		21	1.33	6
(e.2.1)		0.44		39	1.53	27
(e.2.2)		0.73		34	1.33	11
(f.1.1)			0.48	44	1.11	4
(f.1.2)			0.64	40	1.26	10
(f.1.3)			0.96	36	1.52	20
(f.2.1)			0.48	77	1.11	6
(f.2.2)			0.34	75	1.26	17
(f.2.3)			0.96	73	1.52	31

Table X-3-5 Growth time of the Plasma column from the Shell-structures located on both of the contour I and II

τ_S (msec.)	τ_B (msec.)	growth time (msec.)	
		n = - 1.0	n = - 1.3
25	100	63.3	32.8
	250	101.0	46.2
	500	146.1	58.1
50	100	-	49.5
	250	-	71.0
	500	-	90.8

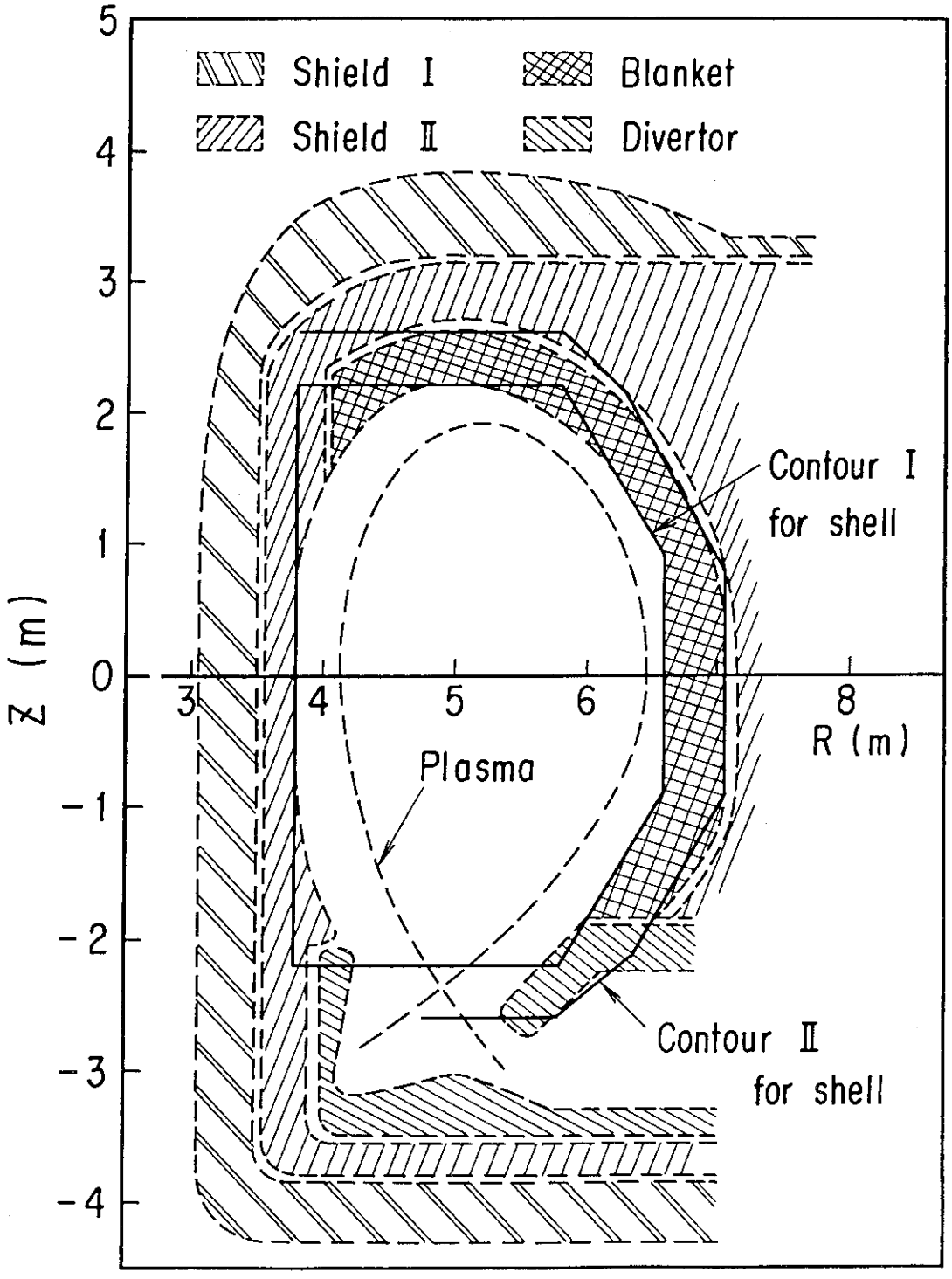

Fig.X-3-1 Structural view nearby the plasma column , and two contours , that is , contour I and II along which shell-structures are located.

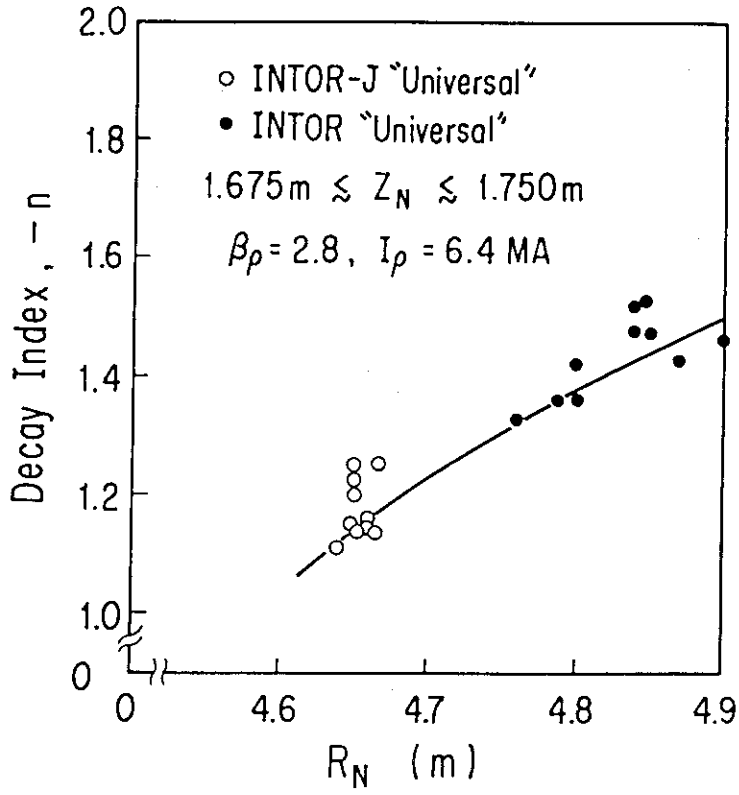

Fig.X-3-2 Dependence of decay index , n upon the radial coordinate , R_N , of active null point in cases of both of the INTOR-J "Universal" and the INTOR "Universal".

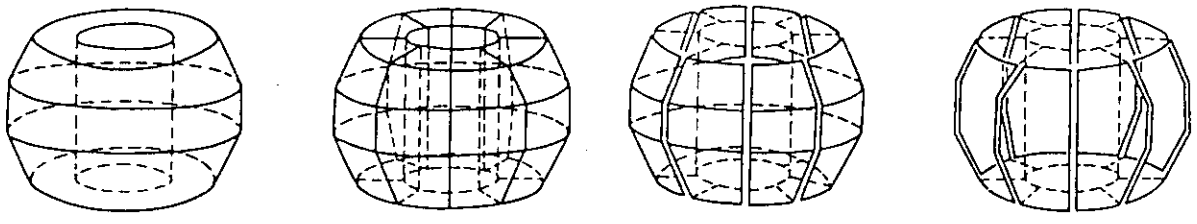

Fig.X-3-3 Various types of shell-structures ; (a) doughnut without cuts, (b) doughnut with cuts , (c) plane ring with cuts , and (d) rectangular coils.

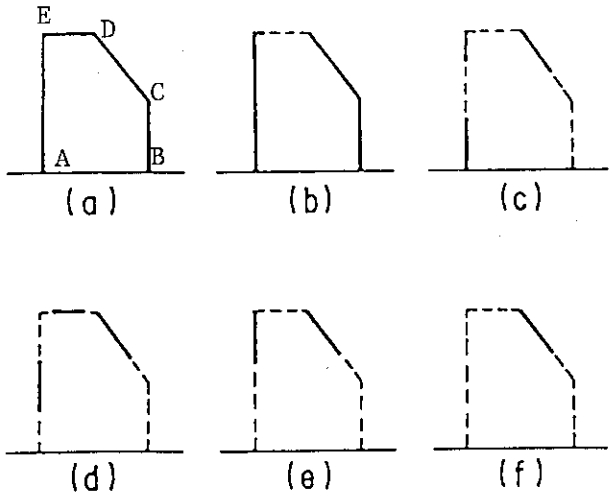

Fig.X-3-4 Various types of plane ring shell-structures. Solid line means plane ring. Coordinates of A is (3.8,0.0) , B(6.6,0.0) , C(6.6,0.9) , D(5.8,2.2) , and E(3.8,2.2).

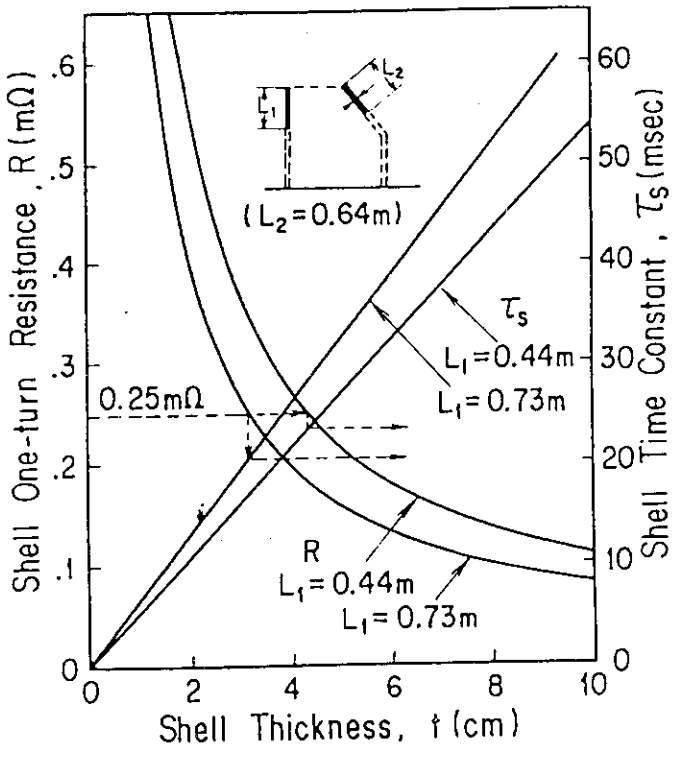

Fig.X-3-5 One-turn resistance and time constant of shell-structure as a function of its thickness in case (e) of Fig.X-3-4. Materials of the shell-structure is stainless steel with $7 \times 10^{-7}\Omega$ m in resistivity.

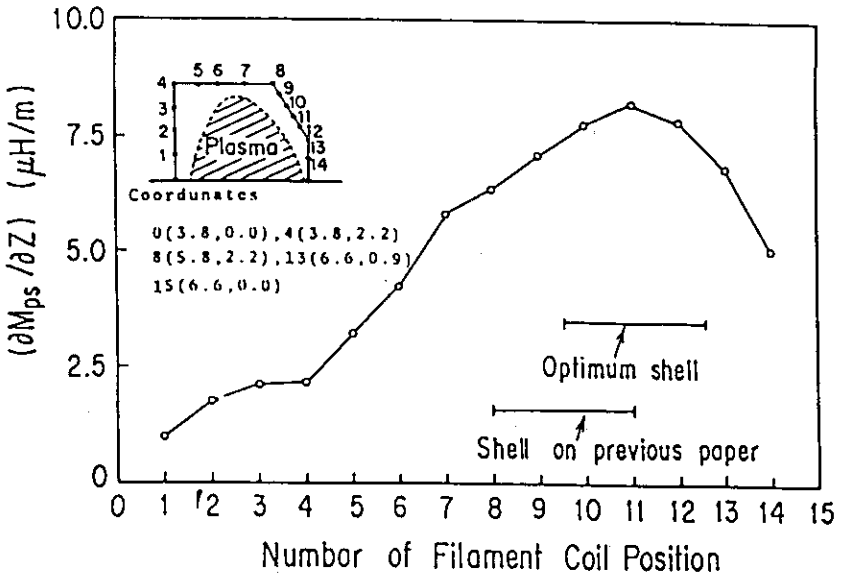

Fig.X-3-6 Dependence of $(\partial M_{ps}/\partial Z)$ upon the location of filament current along the inner surface of plasma vessel.

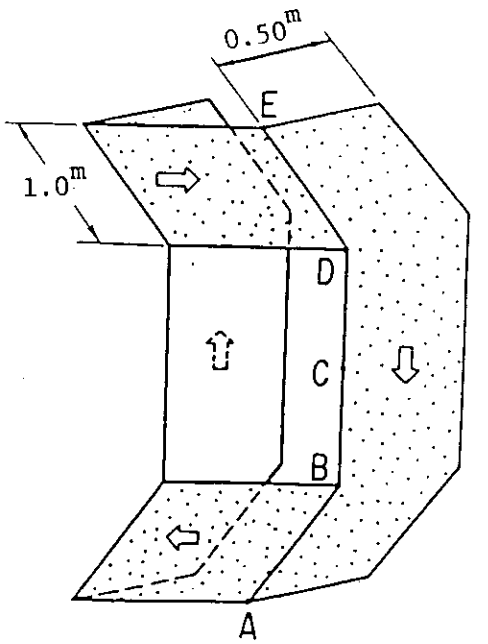

A (6.06^{m} , -1.77^{m}) , B (6.60^{m} , -0.90^{m}) ,

C (6.60^{m} , 0.0^{m}) , D (6.60^{m} , 0.90^{m}) ,

E (6.06^{m} , 1.77^{m})

⇦ : Current Flow

Fig.X-3-7 Structure of a new rectangular shell.

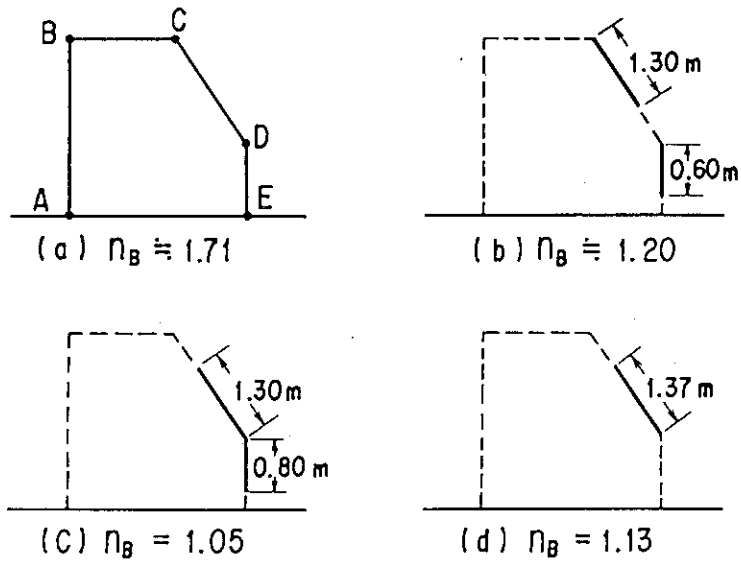

Fig.X-3-8 Various types of plane ring structures located on the contour II. Coordinates of A is (3.8,0.0) , B(3.8,2.7) , C(5.8,2.7) , D(7.1,1.0) , E(7.1,0.0).

4. Active Stabilization and Control

The initial rapid vertical plasma displacement would be stabilized by eddy currents induced in passive components, then, as the induced field is to decay by time constant, the active control coils would be exited to provide the required field for stabilizing a plasma column.

The purpose of this study is to estimate the required power briefly and to seek for the engineering feasibility of the controlability in consideration of the shell effect.

4.1 Vertical

4.1.1 Basic equation

Eq.3.1 — ① can be expressed approximately as the following[A1].

$$Z_p = (R_p/B_0 \cdot n) \cdot \left[\sum_{i=1}^{N} \nu_i I_i + B_d \right] \qquad 4.1 — ①$$

The basic equations, which are related with the vertical position control of a plasma column, are given both of Eq.4.1 — ① and the modified circuit equation,

$$\dot{I}_i + \sum_{j=1}^{N} (M_{ij}/L_i) \cdot \dot{I}_j + (1/\tau_i) \cdot I_i = - \dot{Z}_p \cdot [(\partial M_{pi}/\partial Z)/L_i] \cdot I_p + (V_i/L_i) \qquad 4.1 — ②$$

where the symbols are the same as in section 3.1, and V_i is the applied voltage of the i-th inductive component and is defined as the followings.

$$V_i = 0 \quad \text{(for passive inductive component)}$$

$$= K \cdot [Z_p(t-\delta t) + T_D \cdot Z_p(t-\delta t) + (1/T_I) \int_{t_0}^{t-\delta t} Z_p \, dt] \quad 4.1 \text{ —— } ③$$

(for active inductive component)

where the right hand side of Eq. 4.1 — ③ is the PID (Proportional Integral Differential) controller, K the gain, δt the dead time, to the starting time of control, and T_I and T_D, the time constants of integral and differential circuits, respectively. Additionally, in this paper, δt and t_0 are set on zero, respectively.

4.1.2 Modelled feedback control system

The modelled systems discussed on the rest are two kinds on the followings.

(1) System with the rectangular shells located only on the contour I

This system is composed of 24 rectangular shells, 24 sectors of shields, 24 sectors of blankets and a pair of coils. Its cross-sectional view is given in Fig.X-4-1 where the rectangular shell I and II are shown together, but only the shell I on the contour I is used here. These coils at the top and bottom of the torus are used to produce a horizontal control field and arranged preliminarily at the location in Fig.X-4-1. Each coil has one turn, 0.5 m × 0.5 m in cross-sectional area and they has (3.7^m, $\pm 6.5^m$) on the cylindrical coordinates, respectively. A sector of the shield is divided into two pieces of inside and outside parts by the insulator in Fig.X-4-1, and has about 1.0 m in thickness of stainless steel. A sector of the blanket occupies considerably spacious area in the figure,

but is supposed to have only several cm in effective thickness of stainless steel.

One of 24 rectangular shells is shown in Fig.X-3-7. Its dimension is given together in the figure, too, and it has about 2.0 cm (τ_{shell} = 250 msec) in thickness of copper.

In this case the decay index, n is set -1.0 for the pump limiter. Table X-4-1 shows its circuit parameters with the shells, shields and control coils. In this table the blanket is excluded as it is found that its time constant is less than 10 msec and is roughly one order smaller than the others.

The shield current consists of many current modes but, here, only one current mode, which has the largest derivative with the axial coordinate of the mutual inductance between the plasma and shield, is selected and indicated in the table. Moreover, that modal current results in the largest mutual inductance between the shield and shell, and, similarly, between the shield and control coils. The shield has about 0.172 mΩ in resistance, and about 312 msec in time constant, for the modal current.

The above system (1) is at first studied as the preparatory study for system (2), and in Fig.X-4-2 are shown its typical variations of Z_p, the current and applied voltage, I_{coil} and V_{coil} per a control coil, and the current, I_{shell} of the rectangular shell under the disturbance field which is given by the following.

$$B_d = B_\infty \cdot [1 - \exp(-t/\tau_d)] \qquad 4.1 \text{ —— } ④$$

where B_∞ is the field strength at $t = \infty$ and τ_d its time constant selected 25 msec in the figure.

K and T_I are selected 2.5×10^4 (Volts/m) and 2.5 sec, respectively. Each of Z_p, V_{coil} and I_{coil} is found to have an analogous pattern with these

time variations which has a peak (defined by Z_{MAX}, V_{MAX} and I_{MAX}, respectively) at about 150 msec after start, and is finally damped on a small value. Z_{MAX}, V_{MAX} and I_{MAX} are about 5.8 cm, 1.5 kV and 830 kA, respectively. On the other hand, I_{shell} has a peak and a bottom, that is, about 8 kA at 40 msec and about -6 kA at 300 msec, respectively, and is damped with about 200 msec ($\doteqdot \tau_{shell}$) in e^{-1} time. I_{shell} ahead of the peak keeps the plasma column away from diverging with its initial velocity. The abrupt decrease from the peak to bottom is produced by coupling with the currents of control coils.

In this case, the power, P, required to suppress and control the divergence of the vertical position, is given by $I_{MAX} \cdot V_{MAX}$ and is about 1.25 GW.

(2) System with two kinds of rectangular shells located on both of the contour I and II

This system consists of the shell-structures, located on both of the contour I and II, and two control coils. The shield on the system (1) is found to be excluded from it.

On this more simplified system, the rectangular shell I on the contour I will be selected as thin in thickness of its toroidal bars as possible because of suppressing its influence upon the bleeding ratio by a negligible small. Therefore, the shell effect expected from the shell I is limited within time span shorter than one required for the suppression of the vertical positional instability, and then the rectangular shell II is set so as to compensate its shortage. This system can be realized by employing a concept as shown in Fig.X-4-3.

The shell II has n_B (The subscript B is used for the shell II as well as in Table X-3-5) smaller than n_s (The subscript S for the shell II) on

the shell I, but is selected larger in τ_B than in τ_S nearly by one order.

The positions of two control coils are optimized and selected (6.5^m, $\pm 6.5^m$) on the followings.

(i) On taking the forbidden region for those locations into account

(ii) The control power, P has the following relation.

$$P \propto L_c / \nu_c^2 \qquad 4.1 \text{ —— } ⑤$$

where L_c and ν_c are the self-inductance of a control coil, and magnetic flux density per its unit current, respectively.

Main analyses with this system are given the case of n = -1.30 for the divertor. Also its circuit parameters are shown in Table X- 4-2.

Fig.X-4-4 shows the typical variation of required power (p) with Z_p^{max} on this system. The points of 50 msec in τ_c is obtained on using the PI (Proportional Integral) controller and the others are get from PID (Proportional Integral Differential) controller.

The difference of P between -1.0 and -1.3 in n is very large in Z_p^{MAX} more than 1.0 cm but seems to decrease abruptly in Z_p^{MAX} less than 0.5 cm. These results are thought to be produced from the reason that the shell can play decreasingly effective role with decreasing Z_p^{MAX}. This can be known from abruptly increasing power in comparatively small Z_p^{MAX}.

Also P from the PI controllers is found to be almost the same as from the PID controllers in a range of Z_p^{MAX} shown in the figure.

The system(2) is composed of the least inductive components , the rectangular shells (shell-I and II) and the optimized control coils , and then is thought of giving the least power required for the suppression and control of vertical instability in the INTOR. In practise , inductive components more than in the system(2) are included and will result in more power for its suppression and control under the same disturbance field as in Fig.X-4-4.

4.2 Radial

The study of the active control system for plasma radial displacement, can employ the same method with the vertical displacement.

4.3 Conclusions

Both of the shell effect due to passive shell-structures and the characteristic of simplified feedback control systems, for the vertical position stabilization of the elongated INTOR plasma, are studied and the following matters have been obtained.

Inductive components with the systems consist of shells, shields and control coils. Both of the shells and shield are toroidally divided into 24 sectors.

A new type of retangular shell as shown in Fig.X-3-7 and X-4-3, which has the sufficient shell effect for the stabilization of the fast mode, is presented here on a basis of the studies of various kinds of shell-structures described on this paper in detail, and used as the shell structure.

It is found that the rectangular shells can be formed so as to effect on the bleeding ratio only by a negligible small by locating them separately on the contour I and II defined in Fig.X-3-1.

Some properties with the modelled feedback control system are studied under a disturbance field, $B_d = B_\infty \cdot [1 - \exp(-t/\tau_d)]$ (B_∞: field strength at $t = \infty$, τ_d: time constant). They are studied for two kinds of decay indices, that is, -1.0 for the pump limiter and -1.3 for the divertor.

Conclusively, the control system is found to have good characteristics. The PI controller seems to provide the stable control of the vertical position if the time constant of control coils is selected less than the special value, for example, several tens msec. On the other hand, the PID controller will give its stable control without any constraints for those time constant.

Due to the method in this paper, the maximum of vertical displacement, Z_p^{max} under the disturbance field, B_d, are in proportion to B_∞. Also the power required for its stabilization, P are in proportion to B_∞^2, and therefore $(Z_p^{max})^2$, too. Additionally, A specific power, p ($\equiv P/(Z_p^{max})^2$) is found to be independent to whether the PI or PID controller is used and to be on a curve in relation with Z_p^{max}.

The power in the case of n = -1.0 is found to be about one half times in the case of n = -1.3.

As described on the above, the power is dependent upon $(Z_p^{max})^2$ or B_∞^2 and therefore some common basis will be required for its estimation.

Moreover, P is found to be independent of whether the PI or PID controller is used, and to be on a curve in relation with Z_p^{MAX}. The difference of P between -1.0 and -1.3 in n is very large in Z_p^{MAX} more than -1.0 cm. For example, in the vicinity of $Z_p^{MAX} = 1.0$ cm, P in the case of n = -1.0 is about one half times in the case of n = -1.3. But it seems to decrease abruptly in Z_p^{MAX} less than 0.5 cm.

Table X-4-1 Circuit parameters (System (1))

(μH)

i \ j	1. Shell	2. Shield	3. Coils
1. Shell	46.7	10.48	1.40
2. Shield		53.77	2.68
3. Coils			38.00
$\partial M_{pj}/\partial z(\frac{\mu H}{m})$	− 5.86	− 2.72	− 0.64
$\nu_j(10^{-7}T/A)$	1.77	0.832	0.180
n_j	1.45	0.275	0.010

(1) Plasma Parameters

I_p = 6.4 MA , B_0 = − 0.52

R_p = 5.3 m , n = − 1.0

Table X-4-2 Circuit parameters (System (2))

(μH)

i \ j	1. Shell- I	2. Shell-II	3. Coils
1.Shell-I	46.7	9.96	1.51
2.Shell-II		37.2	2.40
3.Coils			47.1
$\partial M_{pj}/\partial z(\frac{\mu H}{m})$	− 5.86	− 4.62	− 0.62
$\nu_j(10^{-7}T/A)$	1.77	1.39	0.37
n_j	1.45	1.13	0.0145

(1) Plasma Parameters

I_p = 6.4 MA , B_0 = − 0.50

R_p = 5.3 m , n = − 1.30

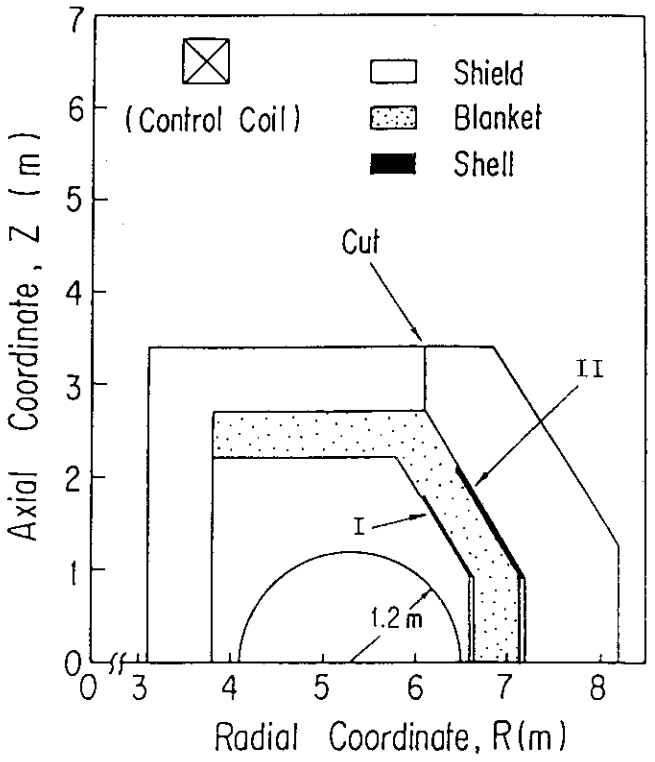

Fig.X-4-1 Vertical cross-sectional view of inductive components used for the modelled feedback control system.

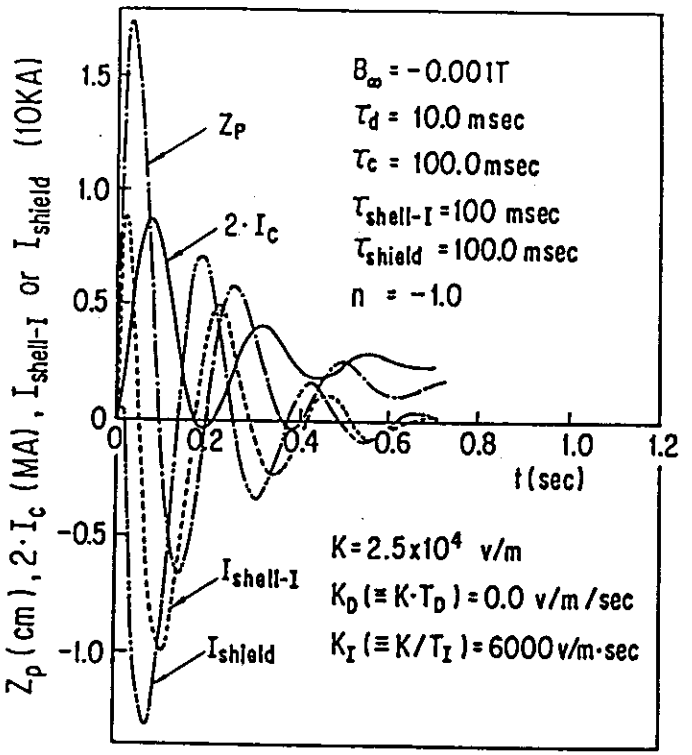

Fig. X-4-2 Typical time evolutions of Z_p, I_c, $I_{shell-I}$ and I_{shield} with the PI controler in case of the system(1)

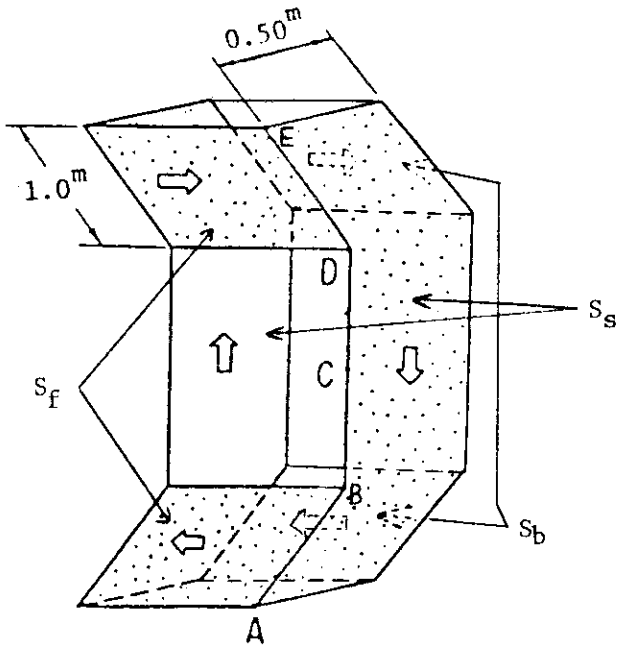

A (6.06m , - 1.77m) , B (6.60m , - 0.90m) ,

C (6.60m , 0.0m) , D (6.60m , 0.90m) ,

E (6.06m , 1.77m)

⇦ : Current Flow

Fig. X-4-3 One of the most favorable shell structures

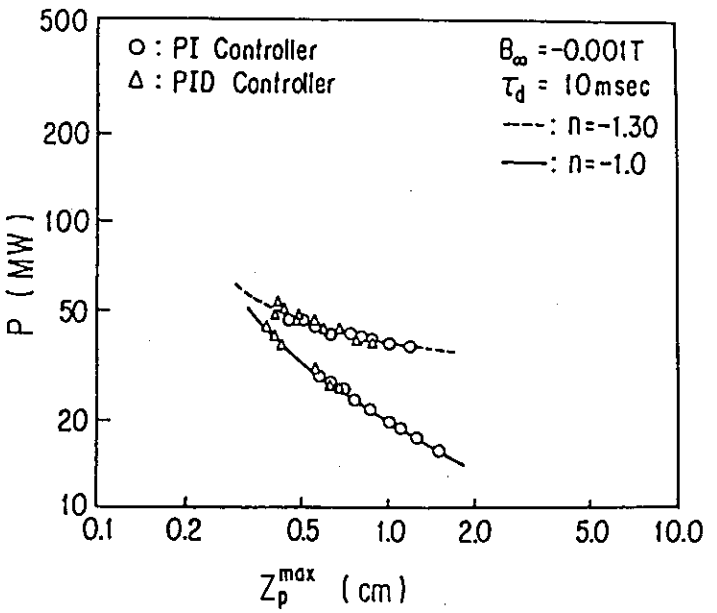

Fig.X-4-4 Dependence of the power , P ,required for the suppression and control of vertical instability upon the maximum vertical displacement , Z_p^{max}, obtained under the disturbance field ; $B = B_\infty \cdot (1.0 - \exp(-t/\tau_d))$, in case of the system(2)

5. Other Studies

5.1 Plasma break-down voltage

The lower break-down voltage will reduce the initial current variation and the induced current on the cryostat. This may reduce the requirement for the power supply system for OH coils.
Detail analysis (which is the relationship between the torus one-turn resistance, the plasma break-down voltage and the required volt-seconds) is required in future to estimate the cost reduction.

5.2 Plasma rise-up time

The slower rise-up of the plasma current will reduce requirement of PF coil power supply. If the rise-up scheme is slowed as in Table X-5-1 and in Fig.X-5-1, from the present current rise-up scheme, (Max. V) x (Max. I) of PF coil system, a good index for the cost of the rectifier and current control system of PF coil power supply, will be reduced to about one-third as shown in Table X-5-2 and higher power factor can be obtained.

Table X-5-1 Plasma current rise-up scheme

I_p (MA)	0 ($\beta_p = 0$)	0.6 ($\beta_p = 0.5$)	5.4 ($\beta_p = 0.5$)	6.4 ($\beta_p = 2.8$)
Reference (BDV=35 V)	0 sec	0.3 sec	5.0 sec	11.0 sec
Slow scheme (BDV 10 V)	0 sec	1.0 sec	10.0 sec	30.0 sec

Table X-5-2 Requirement for PF coil power supply

	Case 2 (Divertor)		Case 4 (Pump Limiter)	
	Reference	Slow Scheme	Reference	Slow Scheme
Peak Power	2742 MW	1405 MW	911 MW	481 MW
Max, Input Engergy	8.2 GJ	8.2 GJ	3.7 GJ	3.7 GJ
(Max.V) × (Max.I)	6.6 GW	2.1 GW	4.0 GW	1.2 GW

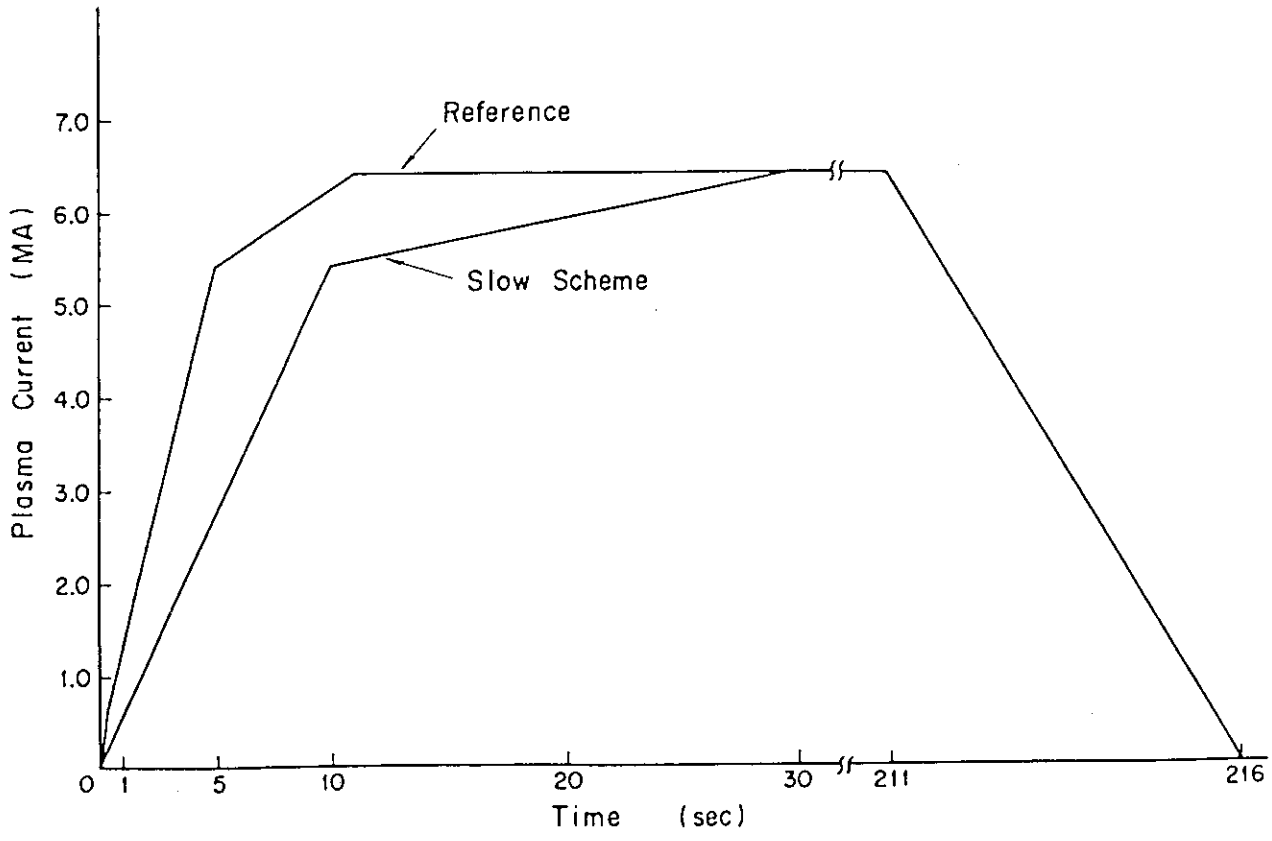

Fig.X-5-1 Plasma current scheme

6. Methodology

Many kinds of electromagnetic phenomenon occur in Tokamak device. In order to increase the calculation efficiency, it is necessary to use a method properly in consideration of the required accuracy. In this section, applied methods in this paper and available methods are briefly described.

6.1 Analytical method for electromagnetic force and joule heating

(1) Rectangular slab in uniform magnetic field (EDYSLAB 1)

ϕ^+, the magnetic potential in positive Z region, and ϕ^-, that in negative Z region, in Fig.X-6-1 are expressed by:

$$\begin{cases} -\phi^+ = \sum_{m=1}^{\infty}\sum_{n=1}^{\infty} A_{mn}(t)\cdot\cos k_m x\cdot\cos k_n y\cdot e^{-k_z Z} + B_z^e(t)\cdot Z \\ -\phi^- = \sum_{m=1}^{\infty}\sum_{n=1}^{\infty} A_{mn}(t)\cdot\cos k_m x\cdot\cos k_n y\cdot e^{k_z Z} + B_z^e(t)\cdot Z \\ k_m = \dfrac{\pi(2m-1)}{a}, \quad k_n = \dfrac{\pi(2n-1)}{b}, \quad k_z = \sqrt{k_m^2 + k_n^2} \end{cases}$$

The time dependence of the coefficient $A_{mn}(t)$ can be solved analytically and the eddy current densities are obtained from the following equations.

$$\mu_0\cdot d\cdot j_x(t) = \frac{\partial}{\partial y}(\phi^+ - \phi^-)\Big|_{z=0}$$

$$\mu_0\cdot d\cdot j_y(t) = -\frac{\partial}{\partial x}(\phi^+ - \phi^-)\Big|_{z=0}$$

d : thickness of the slab

(2) Rectangular bar in uniform magnetic field (EDDYROD)

The magnetic field inside the bar shown in Fig.X-6-2 is described by:

$$B_z(t) = \sum_{m=1}^{\infty} \sum_{n=1}^{\infty} K_{mn}(t) \cdot \cos P_m x \cdot \cos q_n y + B_z^{ex}(t)$$

$$P_m = \frac{\pi(2m-1)}{2a} , \qquad q_n = \frac{\pi(2n-1)}{2b} .$$

The time dependence of the coefficient $K_{mn}(t)$ can be solved analytically and eddy current densities are derived from the following equations.

$$j_x(t) = \frac{1}{\mu_0} \frac{\partial B_z(t)}{\partial y}$$

$$j_y(t) = -\frac{1}{\mu_0} \frac{\partial B_z(t)}{\partial x}$$

(3) Rectangular slab in ununiform magnetic field (EDYSLAB 2)

The eddy current j is defined using the current vector potential V, as represented in Eq.6.1 — ①

$$j = \text{rot } V \qquad 6.1 \text{ —— } ①$$

the relation of V and magnetic field B is derived from Maxwell's equations.

$$\nabla^2 V = \sigma \frac{\partial B}{\partial t} \qquad 6.1 \text{ —— } ②$$

The magnetic field B in the conductor consists of two components, that is, the induced magnetic field by eddy current, B^{in} and the external magnetic field B^{ex}.

B^{ex} in Fig.X-6-3 is

$$B_z^{ex} = \frac{-\mu_0 \cdot I(t) \cdot x}{2\pi(x^2 + Z_0^2)} \qquad 6.1 \text{ —— } ③$$

and Eq.6.1 — ② becomes

$$\frac{\partial^2 V}{\partial x^2} + \frac{\partial^2 V}{\partial y^2} = \sigma \left(\frac{\partial B_z^{in}}{\partial t} + \frac{\partial B_z^{ex}}{\partial t}\right) \qquad 6.1 \text{ —— } ④$$

The Biot-Savalt law is employed to express B_z^{in} by V and Eq.6.1 — ④ results in Eq.6.1 — ⑤.

$$\frac{\partial^2 V}{\partial x^2} + \frac{\partial^2 V}{\partial y^2} = \sigma \left(K \frac{\partial V}{\partial t} + \frac{\partial B_z^{ex}}{\partial t} \right) \qquad 6.1 \text{ — } ⑤$$

The finite-difference equations are available to solve Eq.6.1 — ⑤ and the time variation of current vector potential is obtained by Runge-Kutta method. The following equations are used for calculating eddy current distributions.

$$\left.\begin{aligned} j_x &= \frac{V}{y} \\ j_y &= -\frac{V}{x} \end{aligned}\right\} \qquad 6.1 \text{ — } ⑥$$

6.2 Lumped constant circuit method

(A) RING-I

This code is for determining transient current distribution on a vacuum vessel of tokamak device which has no electric insulation in the toroidal direction. Here, the vacuum vessel is treated as many toroidal conducting rings connected electrically with their mutual inductance. The current distribution (except saddlelike current) on the vacuum vessel is determined from the currents of these rings by solving the circuit equations. By this method, the current distribution of a vacuum vessel with arbitrary cross section can be obtained. The ring model of vacuum vessel is shown in Fig.X-6-4 and the circuit equations can be expressed as follows.

$$V_k = \frac{d\phi_k}{dt} = \Sigma \left(M_{kj} \dot{I}_j + \dot{M}_{kj} I_j \right) \qquad 6.2 \text{ — } ①$$

$$\phi_k = \Sigma M_{kj} I_j \qquad 6.2 \text{ — } ②$$

$$\phi_k = \int V_k dt \qquad 6.2 \text{ —— } ③$$

$$V_k + R_k I_k = 0 \qquad 6.2 \text{ —— } ④$$

And the symbols in above equations are as follows.

M_{kk} ; self inductance of ring k

M_{kj} ; mutual inductance (k and j)

I_k ; current of ring k

R_k ; resistance of ring k

V_k ; one-turn voltage of ring k

ϕ_k ; linkage flux of ring k

Eq.6.2 — ①, ②, ③ and ④ can be rewrited as follows.

$$[M_{kj}]\,[I_k] = [\phi_k] \qquad 6.2 \text{ —— } ⑤$$

$$[I_k] = [M_{kj}]^{-1}\,[\phi_k] \qquad 6.2 \text{ —— } ⑤'$$

$$[\phi_k] = \int [V_k]\, dt \qquad 6.2 \text{ —— } ⑥$$

$$[V_k] = -\,[R_k]\,[I_k] \qquad 6.2 \text{ —— } ⑦$$

From Eq.6.2 — ⑤', ⑥ and ⑦ the electromagnetic phenomenon between plasma and vacuum vessel can be analized.

(B) RING-II

This code is for briefly evaluating the shell effect for passive control in the case of vertical plasma displacement. This function is added to RING-I. The vertical plasma displacement is expressed by using a dipole current model which is shown in Fig.X-6-5 as follow.

$$\Delta S = 2a_p \delta Z \qquad 6.2 \text{ —— } ⑧$$

$$\frac{dI_d}{dt} = \frac{I_p}{\pi a_p^2} \frac{\Delta S}{\delta t} = \frac{2I_p}{\pi a_p} \frac{\delta Z}{\delta t} \qquad 6.2 \text{ —— } ⑨$$

(Uniform plasma current I_p is assumed)

The symbols in Fig.X-6-5 and Eq.6-2 —— ⑧, ⑨ are as follows.

a_p ; plasma monor radius

δZ ; vertical displacement

δt ; spent time for δZ

ΔS ; erea of shadow

I_p ; dipole current

(C) TOKAMAK CIRCUIT [7)]

In this method, the MHD equilibrium theory is taken into the framework of circuit equations. By this method, it is possible to carry out the simulation of the horizontal plasma position, plasma cross section, poloidal magnetic field and the current in the plasma channel and tokamak components through all phase of the discharge: current build-up, flat top and shut down phase (of course it's easy to calculate the induced eddy current at the plasma disruption phase.)

This simulation is useful both in the analysis of plasma behavior and in the design of the feedback system of the plasma current, position and shape. The magnetic flux functions and equations describing the plasma motion and shape are derived from the MHD equilibrium theory[8)]. A model of plasma and vacuum vessel is shown in Fig.X-6-6. The flux function can be easily expressed by currents in the components. For example, the flux function ψ_p by plasma becomes

$$\psi_p = R_p \mu_0 I_p \left(\ell n \frac{8R_p}{r_u} - 2 + \frac{R_p - R_u}{r_u} \cos\omega\right)$$

$$- \frac{\mu_0 I_p}{2} \left[1 - \ell n \frac{8R_p}{r_u} - \frac{r_p^2}{r_u^2} \left(\Lambda_1 + \frac{1}{2}\right)\right] r_u \cos\omega_\rho \qquad 6.2 \text{ —— } (10)$$

(in the first order approximation of the expansion in the inverse aspect ratio)

where

I_p ; plasma current

$\Lambda_1 = \beta_p + \ell_i/2 - 1$

β_p ; poloidal β

ℓ_i ; internal inductance

And, the equation which governs the plasma motion can be readily derived from the flux function following the procedure given by V.S. Mukhovatov and V.D. Shafranov [8].

$$\frac{\mu_0 I_p}{2} \left(\ell n \frac{8R_p}{r_p} + \Lambda_1 - \frac{1}{2}\right) + 2\pi R_p B_z = 0 \qquad 6.2 \text{ —— } (11)$$

Similarly, the equation describing the shape of plasma is

$$\delta + \frac{3r_p^3}{4R_p^2} \left(\ell n \frac{8R_p}{r_p} - \frac{5}{4} - \frac{\Lambda_1}{3}\right) - \frac{r_p^3}{R_p^2} \Lambda_1 - \frac{r_p^3}{R_p^2} \left(\ell n \frac{8R_p}{r_p} - \frac{1}{2} + \Lambda_1\right) n = 0 \qquad 6.2 \text{ —— } (12)$$

where

B_z ; vertical field

n ; n-index $\quad n = - \left[\frac{R}{B_z} \frac{\partial B_z}{\partial R}\right]_{R=R_p}$

while, i_u is set as the current on the vacuum vessel with circular cross section.

$$i_u = i_{u0} + i_{u1}\cos\omega + i_{u2}\cos 2\omega \equiv \frac{I_{u0}}{2\pi r_u} + \frac{I_{u1}}{2r_u}\cos\omega + \frac{I_{u2}}{r_u}\cos 2\omega$$

i_{u0} ; uniform current density

i_{u1} ; dipole current density

i_{u2} ; quadrupole current density

If suffixes I, II mean inside and outside of the vacuum vessel, respectively, the flux functions due to these currents are

$$\psi_u^{I} = \mu_0 R_u I_{u0}\left(\ell n \frac{8R_u}{r_u} - 2\right) + \frac{\mu_0 \pi r_u}{4} I_{u1}\left(\ell n \frac{8R_u}{r_u} - \frac{1}{2}\right)$$

$$+ \frac{\mu_0 \pi}{8r_u} I_{u1}(\rho^2 - r_u^2) + \left\{\frac{\mu_0 \pi R_u}{2r_u} I_{u1} + \frac{\mu_0}{2} I_{u0}\left(\ell n \frac{8R_u}{r_u} - \frac{1}{2}\right)\right.$$

$$\left. + \frac{\mu_0 \pi}{8} I_{u2}\left(2 + \frac{\rho^2}{r_u^2}\right)\right\}\rho\cos\omega + \left(\frac{\mu_0 \pi R_u}{2} I_{u2} + \frac{3\mu_0 \pi r_u}{16} I_{u1}\right)$$

$$\times \frac{\rho^2}{r_u^2}\cos 2\omega \qquad 6.2 \text{ —— } (13)$$

$$\psi_u^{II} = \mu_0 R_u I_{u0}\left(\ell n \frac{8R_u}{\rho} - 2\right) + \frac{\mu_0 \pi r_u}{4} I_{u1}\left(\ell n \frac{8R_u}{\rho} - \frac{1}{2}\right)$$

$$+ \left\{\frac{\mu_0 \pi r_u R_u}{2\rho} I_{u1} + \frac{\mu_0 r_u^2}{4\rho} I_{u0} + \frac{\mu_0 \rho}{2} I_{u0}\left(\ell n \frac{8R_u}{\rho} - 1\right)\right.$$

$$\left. + \frac{3\mu_0 \pi}{8\rho} r_u^2 I_{u2}\right\}\cos\omega + \left\{\frac{\mu_0 \pi r_u^2 R_u}{2\rho^2} I_{u2} + \left(\frac{\mu_0 \pi r_u}{8} + \frac{\mu_0 \pi r_u^3}{16\rho^2}\right) I_{u1}\right\}$$

$$\times \cos 2\omega \qquad 6.2 \text{ —— } (14)$$

and further study[9] in TOKAMAK CIRCUIT enable to consider the saddlelike current if the saddlelike current have been obtained beforehand.

Similarly, the flux functions due to poloidal field coils can be derived.

Mutual inductance can be expressed as follow.

$$M_{mn} I_m I_n = \int_m \psi_n j_m d\ell_m \qquad 6.2 \text{ —— } (15)$$

where suffixes n, n denote the components including plasma. Now, we can describe the circuit equations.

6.3 Distributed constant circuit method

The computer codes of EDDY series have a common theory (method). This method for analizing the eddy current in thin conductors is named 'Finite Element Circuit Method'. The thin conductor is divided into finite elements and the current potential on each element is defined. Electromagnetic coupling constants between current potentials at respective nodes sre calculated by energy integral. And the circuit equations sre calculated by eigen value analysis. The method is easily applicable to conductor of any shape, especially the vacuum vessel, with no limitation by the aspect ratio and the uniform resistance. For example, the bellows of vacuum vessel are assumed to be unisotropic conductive plate.

In order to calculate the eddy current on the periodically symmetric torus with arbitrary shape, EDDYTORS and EDDYACT was developed[4]. The conductive torus is assumed to be made of infinite thin plate with equivalent surface conductivity to the actual torus. Here, the bellows of vacuum vessel is also assumed to be unisotropic conductive plate. The concept of these codes are as follows.

It has been shown that an arbitrary current distribution on the torus can be represented by a current potential $V(\phi,\ell)$, where ϕ is the toroidal angle and ℓ is the poloidal length measured from the outermost point of the torus along the cross section. The toroidal and poloidal component of the current density are given by

$$J_\phi = \frac{\partial V}{\partial \ell}, \qquad J_\ell = -\frac{1}{R}\frac{\partial V}{\partial \phi}$$

here, R is the distance from the symmetric axis of the torus. The current potential can be expanded by the eigen functions $V_n(\phi,\ell)$ as follows;

$$V(\phi,\ell) = \sum_{n=1}^{N} X_n V_n(\phi,\ell) \qquad 6.3 \text{ —— } ①$$

The resistance, self-inductance and decay time constant of the n-th eigenmode are 1, τ_n and τ_n, respectively. The eigenmodes are decoupled with each other.

Supposed that poloidal coils are grouped into M blocks in each of which coils are connected in series, the current, the externally applied voltage, the resistance of m-th block and the mutual inductance between the m-th and m'-th block are I_m, V_m, R_m and $L_{mm'}$, respectively. The flux function on the torus of the m-th block is calculated numerically and represented by $\psi_m(\ell)$. The mutual inductance between the n-th eigenmode and m-th block can be calculated by the integral

$$M_{nm} = \int_{-L}^{L}\int_{0}^{2\pi} \psi_m(\ell)\,\frac{\partial V_n}{\partial \ell}\,d\ell d\phi \qquad 6.3 \text{ —— } ②$$

here, L is the poloidal length from the outermost point to the innermost point of the torus along the cross-section.

Now with these coupling constants, a set of circuit equations are formulated as follows;

$$M\frac{dx}{dy} + RX = \frac{dE}{dt} \qquad 6.3 \text{ —— } ③$$

here

$$X = \begin{bmatrix} X_1 \\ \cdot \\ \cdot \\ \cdot \\ X_N \\ I_1 \\ \cdot \\ \cdot \\ \cdot \\ I_M \end{bmatrix}, \quad E = \begin{bmatrix} 0 \\ \cdot \\ \cdot \\ \cdot \\ 0 \\ E_1 \\ \cdot \\ \cdot \\ \cdot \\ E_M \end{bmatrix}, \quad M = \begin{bmatrix} \tau_1 & & M_{11} & \cdot\cdot & M_{1M} \\ \cdot & & \cdot & & \cdot \\ & \cdot & \cdot & & \cdot \\ & \cdot & \cdot & & \cdot \\ & \tau_N & M_{N1} & & M_{NM} \\ M_{11} & \cdot & M_{N1} & L_{11} \cdot\cdot & L_{1M} \\ \cdot & & \cdot & \cdot & \cdot \\ \cdot & & \cdot & \cdot & \cdot \\ \cdot & & \cdot & \cdot & \cdot \\ M_{1M} & \cdot & M_{N1} & L_{11} \cdot\cdot & L_{MM} \end{bmatrix} \qquad 6.3 \text{ —— } ④$$

and

$$R = \begin{bmatrix} 1 & & & & & & \\ & \cdot & & & 0 & & \\ & & \cdot & & & & \\ & & & \cdot & & & \\ & & & & 1 & & \\ & & & & & R_1 & \\ & 0 & & & & \cdot & \\ & & & & & & \cdot \\ & & & & & & & \cdot \\ & & & & & & & & R_M \end{bmatrix} . \qquad 6.3 \text{ —— } ⑤$$

In the circuit equations, if the m-th block is a current given circuit, I_m is given and E_m should be solved. If the m-th block is a voltage given circuit, E_m is given and I_m should be solved. The plasma loop is a current given circuit. If the plasma position is time-dependent, the mutual inductances between plasma and eigenmodes and/or coil blocks are

time-dependent.

Two of the most advanced calculation codes among EDDY series are EDDYMULT and EDDYARBT.

i) EDDYMULT[5)]

To the demands from a numerical design and control analysis of plasma position, current and its shape, intensive efforts of numerical and analytical eddy current studies have been made in JT-60 project.
The numerical results of eddy current analysis in JT-60 mult-torus system using the numerical code EDDYMULT which was newly developed in JAERI. Taking into account of the mutual coupling between a vacuum vessel, toroidal coils, support plates and a central column, the eigen function of eddy current defined in the entire multi-torus system were obtained by the method of modal analysis[A2].

ii) EDDYARBT[10)]

The numerical method for analyzing transient eddy currents on thin conductors with arbitrary connections and shapes is presented. The eddy currents are described by current functions and discretized in the usual manner of the finite element method. This method is successfully applied to the eddy currents on a sphere surface, a square plate and INTOR-J primary shield. It is shown that this method is accurate and efficient to analyze the eddy currents on complicated conductor structures.

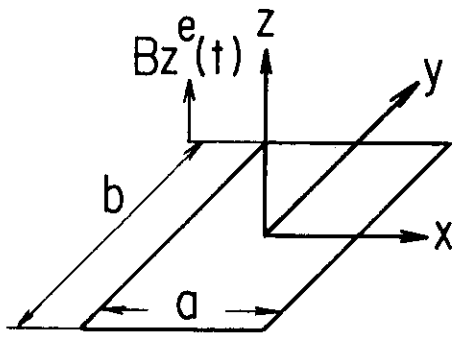

Fig.X-6-1　　Model of EDYSLAB 1

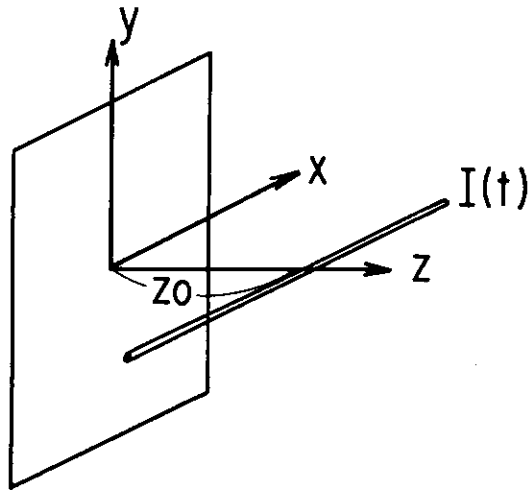

Fig.X-6-3　　Model of EDYSLAB 2

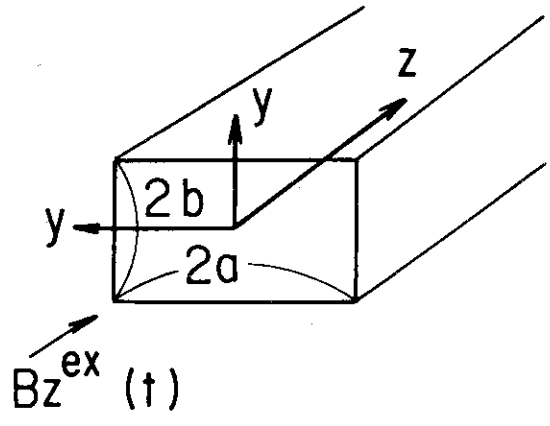

Fig.X-6-2　　Model of EDDYROD

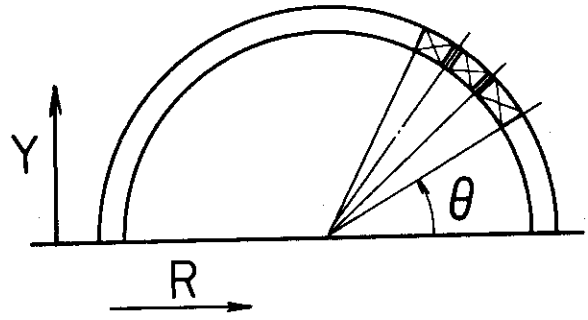

Fig.X-6-4 Ring model of vacuum vessel

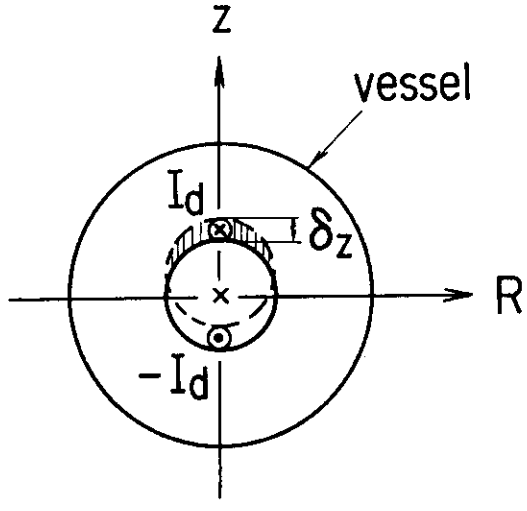

Fig,X-6-5 Dipole current model

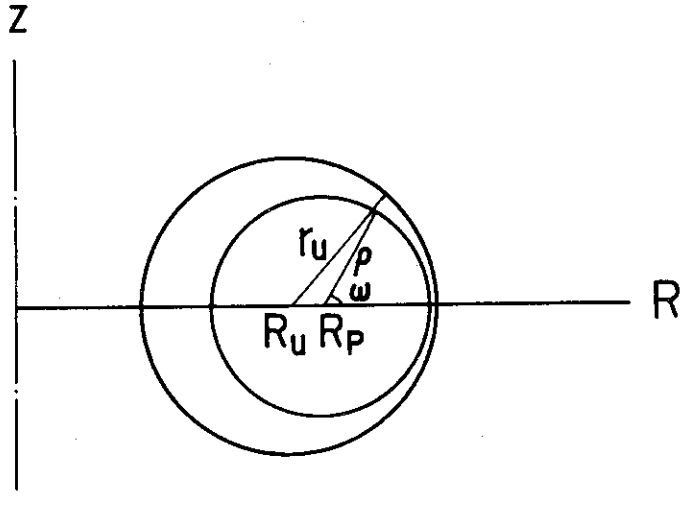

Fig.X-6-6 Model of plasma and vacuum vessel

Acknowledgment

The authers are grateful to Drs. T. Honda, M. Sugihara, A. Kameari, R. Shimada and K. Ebisawa for fruitful discussions. We thank Drs. M. Yoshikawa, K. Tomabechi, Y. Iso and S. Mori for their continuous encouragements.

References

1) A.M. Hassanen et al.: Journal of Nuclear Material, Vol.103, 104 pp.321 (1981)

2) N. Fujisawa, M. Sugihara and K. Ueda: Reports of Physics Group Tasks for IAEA INTOR Workshop, Japan JAERI Mar. 30～Apr. 11 (1981)

3) H. Yokomizo, et al.: JAERI-M 6693 (1976)

4) A. Kameari and Y. Suzuki: JAERI-M 7120 (1977)

5) Y. Nakamura and T. Ozeki: JAERI-M 9612 (1981)

6) K. Sako, et al.: J. Nucl. Sci. Technol., 19(6), 491 (1982)

7) Y. Suzuki, H. Ninomiya, A. Kameari, A. Ogata and H. Aikawa: Japan J. Phys. 16 (1977) 2232

8) V.S. Mukhovatov and V.D. Shafranov: Nuclear Fusion 11, 665, (1971)

9) H. Ninomiya and Y. Suzuki: JAERI-M 7710 (1978)

10) A. Kameari: Journal of Computational Physics 42, 124-140 (1981)

[A1] K. Ueda, S. Nishio, N. Fujisawa, M. Sugihara and S. Saito: to be published for JAERI-M

[A2] Y. Nakamura, T. Ozeki: 12th Symposium on Fusion Technology 13-17 Sept. 1982, Jülich

Acknowledgment

The authers are grateful to Drs. T. Honda, M. Sugihara, A. Kameari, R. Shimada and K. Ebisawa for fruitful discussions. We thank Drs. M. Yoshikawa, K. Tomabechi, Y. Iso and S. Mori for their continuous encouragements.

References

1) A.M. Hassanen et al.: Journal of Nuclear Material, Vol.103, 104 pp.321 (1981)

2) N. Fujisawa, M. Sugihara and K. Ueda: Reports of Physics Group Tasks for IAEA INTOR Workshop, Japan JAERI Mar. 30～Apr. 11 (1981)

3) H. Yokomizo, et al.: JAERI-M 6693 (1976)

4) A. Kameari and Y. Suzuki: JAERI-M 7120 (1977)

5) Y. Nakamura and T. Ozeki: JAERI-M 9612 (1981)

6) K. Sako, et al.: J. Nucl. Sci. Technol., 19(6), 491 (1982)

7) Y. Suzuki, H. Ninomiya, A. Kameari, A. Ogata and H. Aikawa: Japan J. Phys. 16 (1977) 2232

8) V.S. Mukhovatov and V.D. Shafranov: Nuclear Fusion 11, 665, (1971)

9) H. Ninomiya and Y. Suzuki: JAERI-M 7710 (1978)

10) A. Kameari: Journal of Computational Physics 42, 124-140 (1981)

[A1] K. Ueda, S. Nishio, N. Fujisawa, M. Sugihara and S. Saito: to be published for JAERI-M

[A2] Y. Nakamura, T. Ozeki: 12th Symposium on Fusion Technology 13-17 Sept. 1982, Jülich